THE PRECISION ANALYSIS OF TIME SERIES PHOTOMETRY AND ITS APPLICATION TO SEARCHES FOR PRE-MAIN-SEQUENCE OBJECTS

A Dissertation

by

RYAN JAMES OELKERS

Submitted to the Office of Graduate and Professional Studies of
Texas A&M University
in partial fulfillment of the requirements for the degree of

DOCTOR OF PHILOSOPHY

Chair of Committee,	Lucas M. Macri
Committee Members,	Darren L. DePoy
	Jennifer L. Marshall
	Lifan Wang
	James Long
Head of Department,	George R. Welch

May 2016

Major Subject: Physics

ABSTRACT

The past two decades have seen a significant advancement in the detection, classification and understanding of exoplanets and binary star systems. This is due, in large part, to the increase in use of small aperture telescopes ($<$ 20 cm) to survey large portions of the night sky to milli-mag precision with rapid cadence. The vast majority of the planetary and binary systems studied consist of objects on the main sequence or the giant branch, leading to a dearth of knowledge of properties at early times ($<$50 Myr). Only a dozen binaries and one possible transiting Hot Jupiter are known among pre-main sequence objects, yet these are the systems that can provide the best constraints on stellar formation and planetary migration models. The deficiency in the number of well-characterized systems is driven by the inherent and aperiodic variability found in pre-main-sequence objects which can mask and mimic eclipse signals. Nevertheless, a dramatic increase in the total number of systems at early times is required to alleviate the conflict between theory and observation. We have recently completed a photometric survey of 3 nearby ($<$150 pc) and young ($<$50 Myr) moving groups with a small aperture telescope. We discovered over 300 likely pre-main sequence binaries and ruled out 7 possible transiting Hot Jupiters using techniques developed by reducing crowded, defocused images from an analogous system. Using these observations we have determined a lower-limit on the migration timescale for Hot Jupiters to be 11 Myr and have identified numerous high priority pre-main-sequence binary candidates requiring further follow up.

ACKNOWLEDGEMENTS

First and foremost I would like to thank my advisor Lucas Macri. It's impossible for me to express how grateful I am for your friendship over the past 6 years; being your graduate student has been a pleasure. Thank you for always believing in me, even when others did not. I'd also like the thank Darren DePoy for his support and pep talks. I will always remember going to your office with a question and staying to chat for an hour about nothing in particular. Also, thanks for saving my life in Argentina. I'd also like to thank Jennifer Marshall. Thank you for letting me unload my stresses during graduate school and keeping me sane.

I'd like to thank the telescope operators at Bosque Alegre Astrophysical Station: Ceci Quinoñes, Luis Tapía and Pablo Guzzo. You helped keep my dissertation project running and elevated my Spanish speaking skills from a 3rd grade to 5th grade level. I'd also like to thank the support staff at Bosque Alegre for their dedicated hours on the project, especially Ruben Vrecht and Carlos Colazo. I'd also like to thank Diego Garcia Lambas and the University of Córdoba for hosting 'AggieCam'.

Finally I'd like to thank my fellow graduate students while I was at Texas A&M: Mike, Brett, Ben, Katelyn, Steven, Ting, Adam, Jimmy, Heath, Samantha, Dan, Nancy, Wenlong, Yi, Leo, Andrew, Vince and Peter. It was a real treat to have such close co-workers and friends over the years. I'd also like to thank my friends from home, Roman and Natalia, for helping me take my mind off graduate school.

Lastly, I'd like to thank my family: James, Jane, Lauren, Rose, Dylan and Angelique. I would be lost without your support and love. You've always believed in me and you never doubted my abilities, even when I did. And of course, I'd like to thank Miriam for giving me all the love she had. If I've forgotten anyone, thank you.

NOMENCLATURE

2MASS	2 Micron All Sky Survey
α	Right Ascension
AGB	Asymptotic Giant Branch
AGN	Active Galactic Nuclei
ADU	Analog Digital Unit
BLS	Box-Least-Squares algorithm
CCD	Charged Couple Device
CSTAR	Chinese Small Telescope ARray
d	day
δ	Declination
Dec.	Declination
Δ_{90}	90% magnitude range statistic
DIA	Difference Image Analysis
FAP	False Alarm Probability
FFT	Fast Fourier Transform
FoV	Field of View
g	Sloan g filter
h	hour
HAT	Hungarian Automated Telescope
HJ	Hot Jupiter
i	Sloan i filter
IR	infrared
J	Welch-Stetson J statistic

JD	Julian Date
K2	Kepler2
KELT	Kilo-degree Extremely Little Telescope
LS	Lomb-Scargle algorithm
m	minute
mag	magnitude
mmag	milli-magnitude
MJD	Modified-Julian Date
Myr	Million years
P	period
pc	parsec
PMB	Pre-Main-Sequence Binary
PMS	Pre-Main-Sequence
PSF	Point-Spread-Function
r	Sloan r filter
rms	Root Mean Square
R.A.	Right Ascension
RGB	Red Giad Branch
R_J	Radius of Jupiter
s	second
SCP	South Celestial Pole
SDSS	Sloan Digital Sky Survey
SES	Sandiford Echelle Spectrograph
SNR	Signal to Noise Ratio
SPN	Signal to Pink Noise
TFA	Trend Filtering Algorithm

UCAC4	United States Navel Observatory CCD Astrograph Catalog
UV	Ultraviolet
V_{ac}	AggieCam V band
WASP	Wide-Angle Search for Planets
WISE	Wide-field Infrared Survey Explorer

TABLE OF CONTENTS

Page

LIST OF FIGURES

FIGURE Page

LIST OF TABLES

TABLE Page

1. INTRODUCTION

1.1 Time-Series Photometry

Time-series photometry has long been one of the main tools to study many problems in astrophysics. Recent technological advances have enabled a large increase in the number of nearly-uninterrupted, high-quality and high-cadence observations, which has resulted in an increased understanding of stellar astrophysics, the discovery of thousands of exoplanets and the detection of rare transient events (Baglin et al., 2006; Borucki et al., 2010; Law et al., 2009).

In particular, small aperture telescopes have become a dominant force in time-series photometry. Many scientific teams have deployed arrays of small-aperture telescopes because they are are relatively inexpensive, highly reproducible and their wide fields allow for thousands of bright stars to be monitored quickly and efficiently. Additionally, advances in computing power and storage have allowed for the collection of increasingly larger data sets which can be reduced on moderate time scales.

The use of small aperture telescopes has been increasingly beneficial to the detection of exoplanets and the characterization of binary stars. Small telescopes such as HAT, WASP and KELT have all discovered many planets (Bakos et al., 2002; Pollacco et al., 2006; Pepper et al., 2007). Unfortunately, even with the large effort to characterize all known exoplanet systems, there are still outstanding questions about the formation and evolution of these objects and their host stars.

1.2 The Study of Exoplanets

The discovery of the first exoplanet to orbit a main-sequence star (Mayor & Queloz, 1995) was as scientifically exciting as it was puzzling. The large mass of the object (close to that of Jupiter, $\sim 300 M_{\oplus}$) and the extremely close distance

to its host star (< 0.1 AU) presented a challenge to the extant theories of planet formation; many of which were based on the properties of our own solar system. The leading hypothesis to explain the existence of these so-called "Hot Jupiters" (hereafter, HJs) is that they formed beyond the "snow line" of their protoplanetary disks (≥ 4 AU for a Sun-like star) before migrating inwards (Ida & Lin, 2008). However, the timescale for this process has yet to be fully explained theoretically or determined observationally.

The initial discoveries of exoplanets relied on the detection of radial velocity variations in the spectrum of the host star, which arise from the reflex motion due to the presence of a planet. This method requires very precise ($\sigma < 30$ m/s), high signal-to-noise (hereafter SNR) spectroscopy that can only be obtained using complex instruments on moderate to large aperture telescopes ($1 - 10$ m). In contrast, the transit technique can be applied using much more modest telescopes because it relies on the detection of periodic drops in stellar flux that are typically on the order of 1 to 2% for a Jupiter-like planet orbiting a Sun-like star. Both techniques have yielded comparable numbers of confirmed discoveries to date from the ground, with the majority of the transiting planets having been discovered by the *Kepler* space telescope (Exoplanet Orbit Database, February 19, 2016; Borucki et al., 2010)).

The detection of the first planet using the transit method (Charbonneau et al., 2000; Henry et al., 2000) sparked an interest to use the technique on a massive survey scale. Over the past seven years, the *Kepler* and *CoRoT* space telescopes have dominated the field of transiting exoplanet detection, with *Kepler* alone yielding 941 confirmed planets and nearly another 3786 candidates (Exoplanet Orbit Database, (Baglin et al., 2006; Borucki et al., 2010)). The next phase of the *Kepler* mission (called *K2*) has a wide variety of science goals including the study of young stars and exoplanets, AGN variability, asteroseismology and supernovae (Howell et al.,

2014). In contrast, most ongoing ground-based surveys (such as HAT, KELT and WASP; (Bakos et al., 2002), (Pepper et al., 2007), (Pollacco et al., 2006)) target individual bright stars over the entire sky and few surveys have focused on distinct stellar groups or regions for specific science objectives.

1.2.1 Migration Timescales of 'Hot Jupiters'

An excellent understanding of circumstellar disk formation, accretion and dissipation is critical to establish the timescales for planet formation and migration. Yet, the failure to discover authentic HJs around pre-main sequence stars (hereafter PMS) is in sharp contrast with the expectations from migration models (Yu et al., 2015). In this classical model, the gas giants form outside of the 'snow line' while the smaller, rocky planets form inside of this boundary. The snow line is an imaginary line in a planetary system where icy particulates do not receive enough solar flux to sublimate. Therefore, ices can form on growing planetesimals, increasing its mass and allowing the retention of its primary atmosphere. The primary atmosphere is composed primarily of hydrogen and helium and mimics the composition of the proto-planetary disk. Interestingly, these atmospheres are what give the gas giants their large mass, not their rocky cores. Without this larger, rocky/ice mass the primary atmosphere would escape after formation and the planet would remain rocky and low-mass (Ida & Lin, 2008).

It is theorized HJs form outside of the ice boundary and then migrate inwards towards their host star. The expectation from these models is that planetary migration would occur in < 10 Myr since typical planetary disks form, accrete and dissipate on this timescale (Mamajek, 2009). While some theorists have suggested *in-situ* formation for these objects, they have yet to fully explain how the planetesimals could retain their primary atmosphere in the warmer environment within the

snow line (Ida & Lin, 2008).

If disk accretion drives planetary migration, then the planet would need to traverse to the host star before the breakup of the disk, because both types of migration (aptly named Type I and II) rely on the torques provided by disk accretion onto the host star. Type I migration forces the planet inward with the torque caused by the disk's outward spiral density wave. This causes the planet to lose angular momentum and drift inwards towards the host star. Type II migration involves the planetesimal losing angular momentum as material moves across the gaps in the disk left by the planetesimal's formation. A planetesimal is likely to undergo both forms of migration and the transition from Type I to II is expected to be smooth (Ida & Lin, 2008).

Currently, one T-Tauri star ($\sim$ 3 Myr) has been observed to exhibit changes in its light curve that may arise from a transiting HJ (van Eyken et al., 2012). Since its discovery in 2012, many papers have been written supporting and opposing this claim and its confirmation is still up for debate. Therefore, the most reasonable test of planetary models would be a significant increase in the number of detected young HJ candidates.

1.3 The Study of Binary Stars

A wide range of astrophysical studies require an unqualified understanding of the mass and radius of stars. In fact, the two most fundamental parameters in astronomy are mass and radius, yet these can be the most difficult properties to measure. Diverse topics such as planet, star & galaxy formation, the initial stellar mass function, the distance scale and supernovae are just some examples of areas that would benefit from increasingly more realistic stellar evolution models to fully realize the scientific potential of observations. For single stars, astronomers are limited to measuring the luminosities and temperatures and then using a Hertzsprung-Russell diagram,

coupled with stellar isochrones, to infer the masses and radii. Unfortunately, without reliable measurements of stellar masses and radii, these models can be degenerate with other stellar properties.

1.3.1 Measuring Mass and Radius

Fortunately, the study of binary stars can break these degeneracies. A binary (multiple) star system is one which contains two (or more) stars with a shared center of mass. The mass, radius and distance to the system can be directly measured with high accuracy by studying the gravitational effects each star plays on its counterpart.

Binary systems are commonly classified by the method used to discover them:

- Visual Binaries: A system with two stars which can be resolved by the observer and are shown to visibly orbit one another.
- Spectroscopic Binaries: A system where one or two sets of spectral lines exhibit periodic shifts in wavelength.
- Eclipsing Binaries: A system where the light curve shows noticeable drops in brightness due to eclipses from one or more stars.

If spectra are taken throughout the orbit of the binary star types 2&3, the reflex motion of the spectral lines as a function of orbital phase can be used to determine the mass of the two stars. If spectral lines of *both* objects are detected, then the mass of both stars can be determined and the uncertainties on the masses are greatly reduced. Binaries of this nature are called 'Double-lined Spectroscopic Eclipsing Binaries'.

Binary stars which eclipse one another can have their radii measured based on the length of the eclipse, the total orbital period and the speed inferred from the Doppler shift. Accurate and precise measurements of masses and radii rely on robust determinations of the inclination angle of the system.

1.3.2 The Stellar Mass-Radius Relation at Early Times

Precise and accurate measurements of stellar masses and radii at diverse ages, obtained via double-lined eclipsing binary systems, provide the most rigorous tests of stellar evolution models (Torres et al., 2010; Baraffe et al., 2015). Presently, the vast majority of the systems that have been properly characterized contain main-sequence or evolved objects. In contrast, only a dozen pre-main-sequence eclipsing binaries (hereafter, PMB) have been discovered and studied in depth (Morales-Calderón et al., 2012).

Studies of these few PMBs have shown significant differences with predictions, calling into question some of the assumptions adopted by the models. For example, the transformation of observed properties such as temperature and luminosity into mass and age has been shown to be discrepant by $50 - 100\%$ for stars below $1M_{\odot}$; an inconsistency which can only be relaxed by the use of empirical relations (Stassun et al., 2014). As described above, a good understanding of circumstellar disk formation, accretion and dissipation is critical to establish the timescales for planet formation and migration. On a broader scale, the determination of star formation rates is very sensitive to the assumed initial mass function – a parameter that is heavily dependent on the adopted evolutionary tracks of pre-main sequence stars and currently fails to explain the observed distribution of stellar masses (Kennicutt & Evans, 2012). Hence, a significant increase in the number of well-characterized young systems spanning the widest possible range of masses and ages is the best approach to test and eventually improve evolutionary models.

1.4 A Wide-Field Search for 'Hot Jupiters' and Pre-Main-Sequence Binaries

Motivated by the above we completed a wide angle search for HJs and PMBs in order to achieve the following goals:

- Place a limit on the migration time scale of HJs.
- Detect, characterize and prioritize PMB candidates to aid in the constraint of the mass-radius relation.

We employed a wide-field, small-aperture telescope to maximize the number of targets which could be observed at any time and selected 3 young stellar associations to maximize the number of observations which could be taken throughout the year. Before this search could be successful, however, we needed to address the variability of these sources and how to detect low SNR eclipses in such variability.

1.4.1 Pre-Main Sequence Variability

One of the leading reasons PMS stars have been so poorly studied is due to their stellar variability which appears to be both arbitrary and aperiodic. This variability is likely due to the ongoing stellar contraction towards its main-sequence radius, increased spot cycle due to magnetic activity, proto-stellar disk accretion or a combination of all these factors. This variability can mask and mimic signals which are important to the understanding of the fundamental properties of stars; such as determining stellar rotation rates, identifying planetary & stellar eclipses or making precise radial velocity measurements.

Studies attempting to reduce the impact of astrophysical variation in PMS stars rely on the blind whitening of light curves against suspected periodic variability (Kraus et al., 2015) or use of self described, overly flexible data-driven models which de-weight variation similar to the desired signal (Wang et al., 2015). While these techniques adequately remove variation, the possibility that *bona-fide* signals will be removed is greatly increased. Therefore, it is necessary to isolate and understand the source of each signal, prior to removal, in order to preserve the scientific integrity of the data.

2. PRECISION PHOTOMETRY IN HOSTILE ENVIRONMENTS*

We reduced a large ($> 10^6$ images), multi-color (*gri* & *clear*), photometric data set from Dome A in Antarctica to generate and cultivate a highly-precise and effective reduction method which could be used to study PMS stars. The details and results of this study are described below.

2.1 The Chinese Small Telescope ARray

The Chinese Small Telescope ARray (hereafter, CSTAR) was designed to test the feasibility and quality of an observatory stationed at Dome A on the Antarctic Plateau (87.3667°S, 77.3500°E). Dome A is considered to be one of the most promising observing sites on Earth with low temperature (-60 to -80° C), high altitude (4200 m), extremely stable atmospheric conditions (< 0.4 mag extinction for 70% of the time) and nearly-uninterrupted dark conditions for 6 months (Zou et al., 2010; Zhou et al., 2010b; Wang, L. et al., 2011; Wang, S. et al., 2012; Wang, L. et al., 2013; Zhou et al., 2013; Wang, S.-H. et al., 2014; Oelkers et al., 2015). The combination of these factors allow for astronomical observations to take place in nearly space-like conditions. While the primary objective of the telescope was site testing, the initial three years of operations yielded over 10^6 unique photometric data points for $> 10^4$ astronomical sources in *gri* and *clear* filters. Several analyses of this data set have yielded a variety of interesting and rare variable stars such as Blazhko-effect RR Lyraes, exoplanet candidates, eccentric eclipsing binaries, pulsating variables in eclipsing systems and a wide variety of irregular variable sources (Zou et al., 2010;

*Reprinted in part with permission from "Difference Image Analysis of Defocused Observations with CSTAR" by Oelkers et al., 2015. The Astronomical Journal, Volume 149, 50-63 pp., Copyright 2015 by Ryan J. Oelkers and in part with permission from "Stellar Variability and Flare Rates from Dome A, Antarctica using 2009 and 2010 CSTAR Observations' by Oelkers et al., 2016. The Astronomical Journal, accepted, Copyright 2016 by Ryan J. Oelkers.

Zhou et al., 2010b; Wang, L. et al., 2011, 2013; Wang, S. et al., 2014; Qian et al., 2014; Oelkers et al., 2015; Wang, S. et al., 2015; Yang et al., 2015).

CSTAR was deployed to Dome A in early 2008 and carried out observations during three Antarctic winter seasons supported by the PLATO observatory (Lawrence et al., 2009) before being returned to China for comprehensive upgrades in early 2011; the following description applies to the original version of the system. The array was composed of four Schmidt-Cassegrain wide-field telescopes, each with a 145 mm aperture and a field of view (hereafter, FoV) 20.1 sq. degrees. The focal planes contained ANDOR DV435 1K×1K frame-transfer CCDs with a pixel size of 13μm, equivalent to a plate scale of 15$''$/pix. Filters were mounted at the top of the optical tubes, and a 10W electric current was run through a coating of indium tin oxide to prevent frosting (Yuan et al., 2008). Three of the filters were standard SDSS *gri* while the remaining one was a clear filter (hereafter, *clear*). CSTAR contained no moving parts and the telescopes did not track, so as to minimize possible failures during the observing seasons. The telescopes were pointed towards the south celestial pole (hereafter, SCP) and exposures were short (5-40s) to keep the resulting drift from subtending more than a pixel. The telescopes operated unattended with power supplied by gasoline engine generators (Yuan et al., 2008; Zhou et al., 2010a).

During the 2009 winter season, observations were carried out by the telescopes equipped with *g*, *clear* and *r* filters. The remaining telescope, equipped with an *i* filter, failed to return data. The observations spanned MJD 54935-85 in *g* & *clear* and MJD 54910-5143 in *r* and exposure times varied between 5−20 s. Oelkers et al. (2015) identified significant operating issues with the telescopes during the 2009 observing season. The primary obstacle for this data reduction was a defocused point-spread function (hereafter, PSF). The PSF widely varied between regular torus-like shapes and irregular extended torus shapes blending multiple point sources. Figure 2.1

shows an area of each 2009 master frame. The *clear* telescope also suffered from severe intermittent lens frosting which led to the loss of $\sim 40\%$ of the data. The r telescope suffered from computer problems between MJD 54910-55 that resulted in incorrect exposure time information and images in which only part of the CCD appeared to be fully illuminated. Despite the removal of the affected data, $\sim 8 \times 10^5$ scientifically useful images were acquired over 125 days (Oelkers et al., 2015).

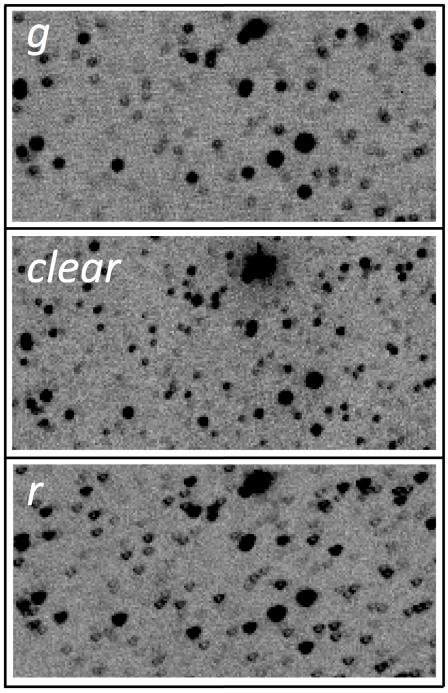

Figure 2.1: 2009 CSTAR Reference Frames
200×100 pixel subsections of each reference frame in g(top), *clear* (middle) and r (bottom), all centered on the south celestial pole (SCP). Each frame shows the varying level of defocusing in each telescope, giving rise to the donut-shaped PSFs. The color has been inverted for clarity, with darker colors denoting more positive flux.

During the 2010 winter season, observations were only carried out with the telescope equipped with the i filter since the other telescopes failed to return data. The reduced observations spanned MJD 55317-5460 with exposures times of $20 - 40$ s. No major observing complications were identified in previous reductions or in this analysis.

2.2 Data Processing

2.2.1 Flat Fielding and Bias Subtraction

The first step in pre-processing images is the subtraction of a bias frame and the generation of an accurate flat field. The bias frame tracks the pixel-to-pixel structure of the read noise across the image. A full bias frame needs to be subtracted from each image because the bias structure varies across the image. Bias frames are generated by reading out the CCD with an exposure time of zero seconds. Typically, multiple bias frames are generated and then median combined to best estimate the true pixel-to-pixel variation. The flat field tracks the pixel-to-pixel structure of the detector's sensitivity to incoming photons. The sensitivity will vary across the detector because the optics will refract the photons as they enter the system and not uniformly illuminate the CCD (this is known as vignetting) and because the detectors do not have perfect quantum efficiency across their surface due to small imperfections. A flat field is generated to correct for these variations by median combining uniformly well-illuminated images and normalizing by the mode of the pixel values. All images are then normalized by this flat field.

We used bias frames obtained during instrument testing in China (Zhou et al., 2010a) while sky flats were generated from our observations. We selected $\geq$ 3000 frames where the sky background was higher than 7,000, 4,000 and 10,000 ADU for the g, r and i flats, respectively; the corresponding values for *clear* were $\geq$

8000 frames and 10,000 ADU. We bias-subtracted, scaled and median-combined the selected frames to make a temporary flat field, applied it to the images, masked any detected stars and repeated the process to generate the final flat fields.

During this process, structure was found in the *clear* images, which was determined to be the result of partial-to-complete frosting of the filter. Quantitatively, this can be seen in the variation of the number of sources recovered in each frame after flat fielding, as shown in Figure 2.2. The number of sources increases once the exposure time is increased from 5 to 20 seconds, 25 days after the start of observations. The number of stars drops dramatically $\sim$ 10 days later, signaling the advanced stages of filter frosting. We removed $\sim 40\%$ of all *clear* frames after MJD 54945, when the star counts dropped below 3000/frame. We later removed another $\sim 25\%$ of the remaining *clear* frames in which all light curves exhibited a significantly higher dispersion (~ 0.2 mag or greater), which we interpreted as evidence of intermittent frosting (see Figure 2.2 for details).

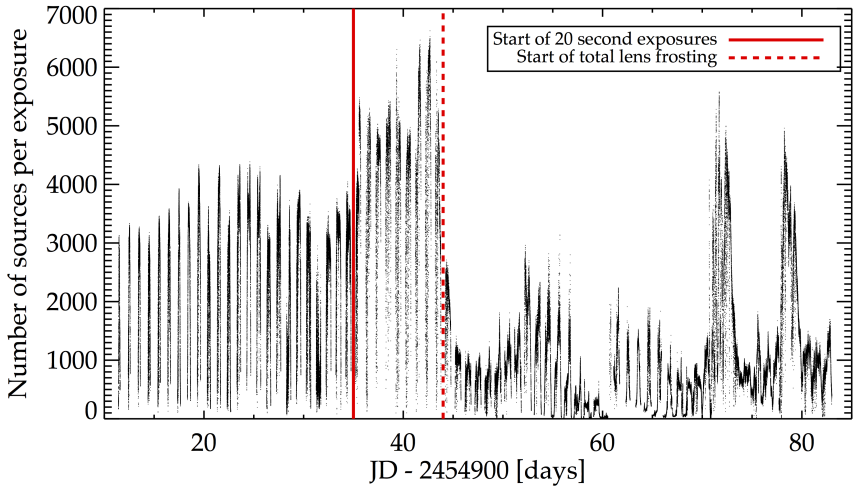

Figure 2.2: Number of Sources in *clear* Band
The number of detected sources with the DAOPHOT, FIND (Stetson, 1987) routine for *clear* as a function of Julian date. The number of stars per exposure remains somewhat constant until $\sim$ 10 days after the switch from 5s exposures to 20s exposures signifying filter frosting.

2.2.2 Background & Electronic Pattern Subtraction

After flat fielding, some frames still exhibited a low-frequency residual background, likely due to moonlight or aurora. We applied a residual background subtraction following the approach of Wang, L. et al. (2013). The residual background model is constructed by sampling the sky background every 32 pix in x&y over the entire detector. Bad or saturated pixels are excluded from each sky sample. A model sky is then fit and interpolated using a thin-plate spline, and then subtracted from each image (Duchon, 1976). We used the IDL routine GRID_TPS for this procedure.

Images in all bands exhibited a similar electronic noise pattern which became significant at low sky background levels. We used the following procedure to remove

the pattern. All stars at 2.5σ above the sky level and all bad pixels were masked and replaced with random values based on a Gaussian distribution that matched the properties of the background. We calculated the Fast Fourier Transform (hereafter, FFT) of each image and identified significant peaks with a power greater than 10^{-3}, which corresponded to the frequency of the electronic pattern. We generated an image containing the unwanted pattern by taking the inverse FFT of the selected frequencies, which was subtracted from the original image. This process was carried out separately for each frame, since the pattern shifted from image to image.

2.2.3 Frame Alignment

Difference imaging requires precise frame alignment in order to produce a proper subtraction. Since CSTAR had fixed pointing towards the SCP it was necessary to rotate each image to match the orientation of its reference frame. We initially used the difference between the date of each target image and the reference frame to calculate the angle offset. We rotated each frame using a cubic convolution interpolation that approximates the optimum interpolation function, as implemented in the IDL function ROT. This function can optionally apply a translation to the target image.

As seen in previous reductions of CSTAR data, we found that the time stamps generated by the local computer drifted as the season progressed, leading to improper alignment of the frames and poor image differencing. This drift was expected due to the lack of network time synchronization at Dome A. Furthermore, we noticed that the location of the SCP (determined from the astrometrically-calibrated master frame of Wang, L. et al. (2013)) moved across the detector as a function of time. While the exact nature of this motion has yet to be determined, it is hypothesized to be due to the drift of the Antarctic ice shelf, the effect of winds, heating due to changes in solar elevation, or a combination of these.

We solved both issues by carrying out aperture photometry on all images and matching star lists using the DAOPHOT, DAOMATCH and DAOMASTER programs (Stetson, 1987). Once the proper rotation and translation values were determined for each image, they were applied using the function described above. Figures 2.3 & 2.4 show the displacement of the SCP from its initial position as a function of time for the g & i images. Using a Lomb-Scargle [LS] periodogram (Lomb, 1976; Scargle, 1982), we found 2 significant periods at 1 and 28.8 days; these two periods are likely due to changes in solar elevation & lunar tides, respectively. We also identified a significant period at 10.5 d during the 2010 winter season.

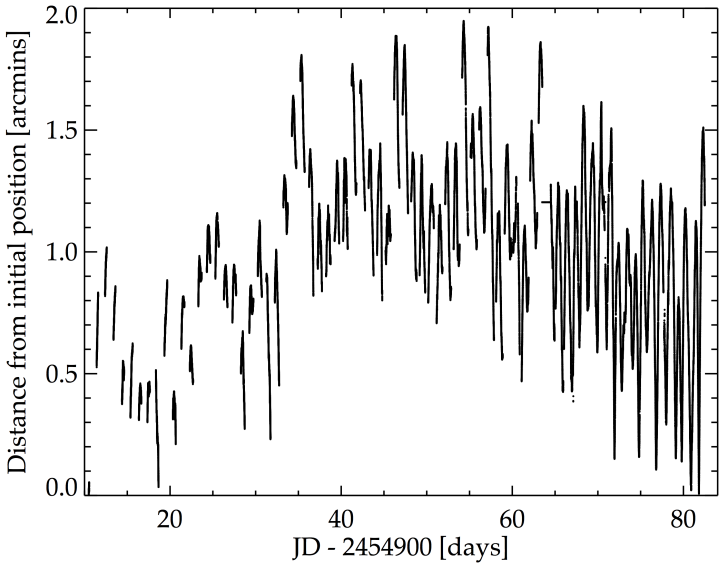

Figure 2.3: The Movement of the SCP in g
The movement if the SCP from its initial position in g as a function of Julian date. There are variations in the movement of the SCP both on a daily level and with a period of 28.8 days.

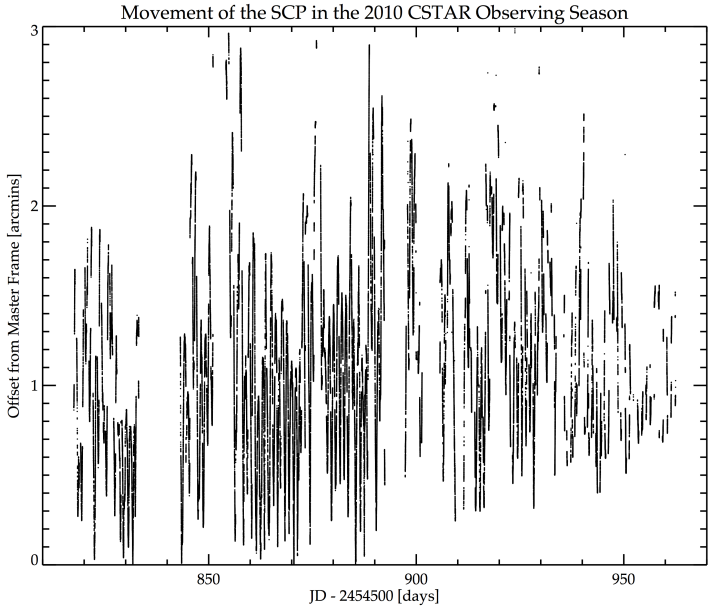

Figure 2.4: The Movement of the SCP in i
The movement of the SCP from the position in our reference frame in i as a function of Julian date. There are variations in the movement of the SCP both on a daily level and with a period of 10.5. We hypothesize these periods are due to the changes in the solar elevation, wind, movement of the ice shelf or a combination of all of these.

2.2.4 Aperture Photometry vs PSF Photometry

Aperture photometry involves the placement of apertures of fixed radii on the centroid of a target star, summing the enclosed flux, and correcting for background light estimated from an annular region. Aperture photometry works best when the ratio of PSF size to stellar separation is well below 1; in other words, when blending and crowding are not significant. Previous analysis of CSTAR data (Zou et al., 2010; Zhou et al., 2010b; Wang, L. et al., 2011, 2013) were based on aperture photometry. However, the 2009 CSTAR data did not meet these standards, making

the use of aperture photometry undesirable. We therefore elected to use difference image analysis (hereafter, DIA) to measure our photometry.

2.2.5 Difference Imaging Analysis

We used DIA to measure changes in stellar flux between each science frame and a reference frame. DIA has been shown to work well in crowded fields with data from small-aperture telescopes (Pepper et al., 2007). DIA involves the convolution a high-quality reference frame with a kernel to match the PSF of a lower-quality science frame as represented in the equation below:

$$D(x,y) = S(x,y) - R(x,y) * K_{\alpha,\beta}(u,v) \tag{2.1}$$

The PSF of a ground-based image (commonly reffered to as "seeing") is determined by atmospheric conditions at a variety of altitudes. The convolution kernel is typically best represented by a shape similar to the PSF of the detector. The most popular DIA routine is *ISIS* (Alard & Lupton, 1998), where the kernel is defined as the combination of 2 or more Gaussian profiles. While effective at modeling well-defined, circular PSFs, this kernel has difficulty properly fitting other PSF shapes. Therefore, we used a Dirac-δ function kernel to compensate for our non-circular, irregular PSF shape. We redefined the kernel as

$$K(x,y) = \sum_{\alpha=-w}^{w} \sum_{\beta=-w}^{w} c_{\alpha,\beta}(x,y) K_{\alpha,\beta}(u,v) \tag{2.2}$$

where $K_{\alpha,\beta}$ is a combination of $(2w+1)^2$ delta function basis vectors and $K_{0,0}$ is the centered delta function (Miller et al., 2008). We redefined our basis vectors to ensure a constant photometric flux ratio between images (Alard, 2000; Miller et al., 2008). In the case of $\alpha \neq 0$ and $\beta \neq 0$,

$$K_{\alpha,\beta}(u,v) = \delta(u-\alpha, v-\beta) - \delta(u,v) \tag{2.3}$$

while for $\alpha = 0$ and $\beta = 0$,

$$K_{0,0}(u,v) = \delta(u,v). \tag{2.4}$$

Stamps were taken around bright, isolated stars to solve for the coefficients $c_{\alpha,\beta}(x,y)$ using the least-squares method. Since the PSF in our images was spatially varying, we applied a 5×5, 1^{st}-order adaptive kernel across the frames. We found this kernel size minimized the χ^2_ν solution *without* over-fitting the data as shown in Figure 2.5. We also allowed $c_{0,0}(x,y)$ to be spatially variable to compensate for imperfect flat field corrections. The typical quality of the differencing for each band in shown in Figure 2.6.

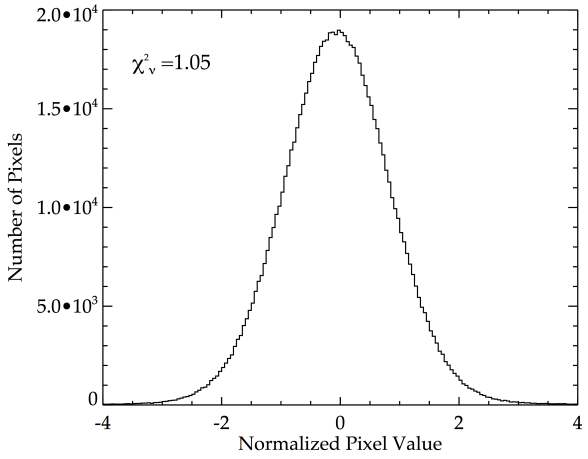

Figure 2.5: χ^2 of Normalized Residuals
The normalized distribution of pixel values for an average differenced frame. We excluded pixels near stars close to saturation or near to the edge of the frame. A proper subtraction should yield $\chi^2_\nu \sim 1$; this frame has $\chi^2_\nu = 1.05$.

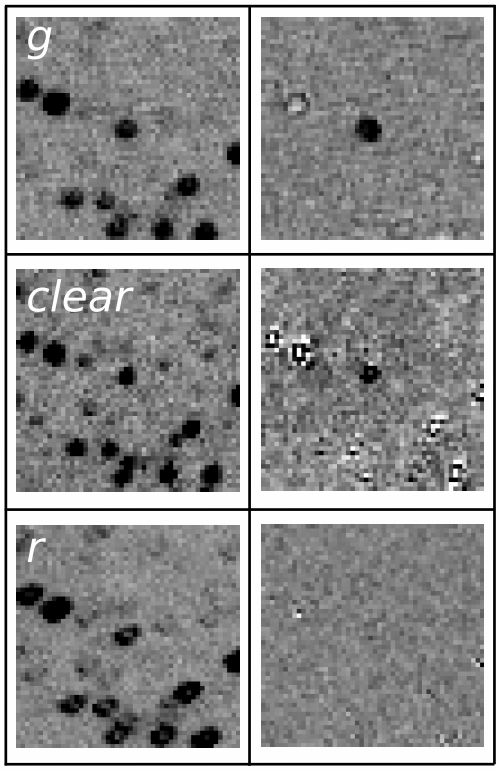

Figure 2.6: Example of Differenced Images

50×50 pixel subsections of each reference frame (left) and 3 differenced science frames (right). Each subsection is centered on a recovered RR Lyrae #n058002 in g (top), *clear* (middle) and r (bottom). The right frames show differenced frames at varying points of the RR Lyrae phase. g shows the star at maximum, *clear* shows the star at mid brightness and r shows the star at minimum. Coincidentally, the reference frame was obtained at the time of minimum light for the RR Lyrae and thus no change appears in the last differenced frame instead of a negative value. Systematics can be seen in the *clear* differenced frame due to the lens frosting. Each frame has a pixel scale of $15''$/pix. The color scale has been inverted for clarity, with darker colors denoting a positive residual.

2.2.5.1 Reference Frame

A key component to DIA is the generation of a high-quality reference frame. Typically this frame is generated by median-combining many individual frames with high SNR and the best seeing, obtained throughout the observing season. For the 2009 CSTAR data this approach is not feasible due to the spatial variations in the defocused PSFs and the continuously changing orientation of the field. When we carried out this process we found the PSF of the reference frame became broader and more Gaussian-like in shape compared to the torus-like PSF of individual images, making it more difficult to convolve and subtract. Therefore we selected a single frame obtained near the end of the observing season (free of satellite trails, clouds or other undesirable features) as the reference for each band. Subsections of the reference frames are shown in Figure 2.1. Unfortunately, unlike using a median combination of images, using a single image as a reference frame does not minimize the possible noise in the reference. However, because the frame was selected to be of better or equal quality than the science frames, we expect the photometric uncertainty will not increase by more than $\sim \sqrt{2}$. The 2010 i reference frame was created by median combining over $3,500$ images with $> 10^4$ stars and a background level below 400 ADU.

2.2.6 Flux Extraction

Master star lists were created by first transforming the coordinates of all sources in Wang, L. et al. (2013) to each reference frame. These positions were masked and the DAOPHOT-FIND routine was run to search for any additional stars which might have been missed in the previous work. We repeated the masking and search steps one additional time to increase completeness at the faint end. We initially removed stars with $< 50,000$ data points or which had an rms> 0.75 mag. The star lists where

then matched using the positions from DAOMATCH and DAOMASTER. The final star lists consist of 5,846, 12,782 & 10,672 stars in *gri*, respectively for a total of 15,380 stars, with 6,072 sources in at least 2 bands.

We found 292 stars in g and 1959 stars in r to match to multiple stars in i because of the defocused PSF in the 2009 data set. We kept each match and flagged the appropriate stars in the stellar library described in § 3.5.1. This is shown with the MATCHING flag in Table 2.1 with either a 0 (no multi-match) or 1 (multi-match). Similarly some stars in g & r, show magnitudes significantly brighter than would be expected for typical g-r or r-i colors. This is likely because the aperture magnitudes in the 2009 reference frames likely caused an increase in flux in both bands for some crowded stars. Stars with possible contamination are also flagged in the library with the CROWDING flag with either 0 (normal) or 1 (possible contamination).

We extracted differential fluxes using aperture photometry with the IDL version of the DAOPHOT package. We set the radius for the photometric aperture at 2.5 and 5 pixels ($37.5''$ and $75''$) for i and $g\&r$, respectively, with sky annuli spanning $4-6$ and $8-10$ pixels ($1-1.5'$ and $2-2.5'$) in each case.

Table 2.1: CSTAR Difference Image Library

CSTAR ID	RA	Dec	g	r	i	Variability	Periodicity	Transit	Type	LS-Period	BLS-Period	Crowding	Matching
CSTARJ092823.53-882925	09:28:23.53	-88:29:25	12.227	12.065	11.733	4	4	0	RR	0.621805	...	0	1
CSTARJ142823.83-883839	14:28:23.83	-88:38:39	12.589	12.624	12.115	4	4	0	RR	0.646542	...	0	0
CSTARJ064036.43-881422	06:40:36.43	-88:14:22	12.095	11.960	11.727	4	4	0	EB	0.438630	...	0	0
CSTARJ084537.33-883343	08:45:37.33	-88:33:43	13.175	12.570	11.996	4	3	2	EB	0.267132	0.267063	0	0
CSTARJ092839.06-882923	09:28:39.06	-88:29:23	12.547	12.065	11.929	4	4	0	RR	0.621802	...	0	1
CSTARJ092021.89-884428	09:20:21.89	-88:44:28	11.235	10.536	10.079	3	2	0	PR	7.29665	...	0	1
CSTARJ111627.63-883533	11:16:27.63	-88:35:33	12.014	10.984	9.386	3	0	0	LT	...	...	0	0
CSTARJ025837.50-880223	02:58:37.50	-88:02:23	12.688	12.503	13.722	3	2	0	IR	0.199018	...	1	0
CSTARJ182819.56-883244	18:28:19.56	-88:32:44	13.751	13.447	13.336	3	4	0	RR	0.572977	...	0	0
CSTARJ024229.86-880426	02:42:29.86	-88:04:26	12.238	11.220	9.466	3	0	0	LT	...	...	0	0
...	...	...	...	...	...	...	...	...	...	...	...		

We applied an exposure time correction based on the given exposure times in the image header. However, this did not properly scale the flux for r exposures taken between MJD 54910 and 54955. We determined the effective exposure times for these images as follows. We measured the peak magnitudes in successive cycles of previously-known contact binaries and RR Lyraes (since their variations are known to be highly stable) and compared those values to the ones measured on the day when our reference images were obtained. We determined that images taken between MJD 54910 and 54935 had exposure times 5× shorter than expected, while those obtained between MJD 54935 and 54955 had exposure times 4× shorter than expected. We hypothesize that the telescope was commanded to expose for 5 or 20 seconds during the respective time intervals but actually exposed for 1 and 5 seconds, respectively. We therefore adopted the latter exposure times in our analysis. We scaled the DAOPHOT errors to match what was expected based on the new exposure times and the error after MJD 54955 to ensure they would not be underestimated.

Finally, we applied an absolute photometric calibration based on the synthetic $griz$ magnitudes of Tycho stars from Ofek (2008) following a similar method to previous reductions (Wang, L. et al., 2011, 2013). The *clear* photometry was calibrated to the Tycho V_T system (Grossmann et al., 1995). We used the relations from Wang, L. et al. (2013) to correct for the time drift of the acquisition computer in the 2010 data. Finally we removed measurements with large photometric errors and scatter, likely due to cosmic rays or bad subtractions, if these exceeded $+4\sigma$ of a moving median.

2.2.7 Trend Removal

We used the ensemble photometry to identify and remove systematic trends due to instrumental or processing effects that were present in multiple light curves. These systematics could have several origins as described in detail in the next section. The first is due to the movement of the stars around the detector, due to small residual variations in quantum efficiency or improper flat-fielding. Convolving the reference frame with a kernel matrix could also introduce systematics if the kernel was improperly solved. Finally, lens vignetting, subtle changes in the airmass across the wide field and filter frosting may create non-astrophysical fluctuations in the light curves.

We used the Trend Fitting Algorithm (TFA) in signal reconstruction mode (Kovács et al., 2005) as implemented in the VARTOOLS package (Hartman et al., 2008) to compensate for these systematics. We used 150 stars spanning a wide range of fluxes and locations in the frame that did not exhibit any discernible variations of an astrophysical nature (e.g., eclipsing binaries, periodic variables, etc.) as templates for the trend removal.

We also implemented an alternative trend-removal procedure to deal with the unusual systematics that may arise from the unique nature of the CSTAR observations, namely stars that describe a daily circular motion across the FoV. We ran a Lomb-Scargle (Lomb, 1976; Scargle, 1982) period search on every light curve and identified its most significant period within $0.98 < P < 1.02$ d. We selected the equivalent of TFA reference stars with the same period as the target object, light curve rms$<$ 0.2 mag, and located within 110 pixels in radius of the object being considered. Each reference star was scaled to match the amplitude of the variation in the target star. All of the resulting scaled reference light curves were median com-

bined and subtracted from the target light curve. Stars known to exhibit periodic variations of astrophysical origin had this signal removed (a process commonly referred to as pre-whitening) before conducting this correction. We calculated the rms on 30-minute timescales for the light curves corrected with TFA and the alternative approach and selected the one that exhibited the lowest dispersion.

The combination of robust aliasing removal and use of DIA yielded light curves with lower dispersion than previous analyses of the 2010 CSTAR data, which were based on simpler aperture photometry. We find the rms with DIA to be lower by $\sim$ 9 mmag for stars with $i<$ 11 as compared to the same stars with aperture photometry, as shown in Figure 2.7.

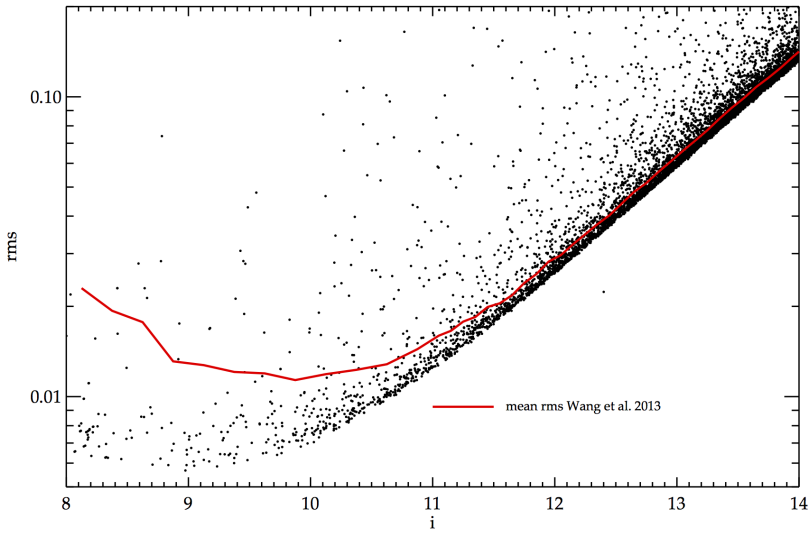

Figure 2.7: DIA Photometry vs. Aperture Photometry
A comparison of the rms from this work and the rms of Wang, L. et al. (2013). The black points mark the rms for stars in the 2010 data set reduced with DIA. The red line is the mean rms of Wang, L. et al. (2013) at each magnitude. This work achieves a lower rms for stars $i<$ 11 by 9 mmag and is consistent with the previous work at fainter magnitudes.

2.3 Systematic and Statistical Uncertainties in Photometry

Small-aperture telescopes may exhibit enhanced systematic effects that are present in their larger counterparts, especially when considering the effects of a defocused PSF. Flat-fielding errors, bad subtractions, misalignments and ghost reflections are all examples of sources creating features in light curves which can mimic true signals. When a star is isolated and free from the effects of crowding and blending, purposefully defocusing a telescope has been shown to greatly decrease the photometric dispersion by minimizing flat-field uncertainties (Southworth et al., 2013). The unanticipated defocusing of the CSTAR system presented difficulty as the telescope was not designed for such techniques due to its crowded field and large pixel scale. Adequate understanding of noise is key to understanding the difference between true signals and systematics. We employed several methods, described below, to decrease the impact these systematics played on our data reduction and detection metrics.

2.3.1 Known Systematic Fluctuations

2.3.1.1 Bad Subtractions due to High Attenuation

DIA uses the least-squares method to find the zero point offset between science frames and a reference frame. In theory, changes due to airmass and the cloud layer should be removed with a proper kernel solution. However, we found that high levels of attenuation due to frosting or clouds (> 1.5 mag) significantly decrease the SNR of the brightest stars and the number of possible kernel template stars, leading to significant subtraction artifacts. Therefore, we removed any images with < 1300 stars in the central 512×512 pix. This led to a reduction in the dispersion of each light curve by $\sim 0.005 - 0.02$ mag.

2.3.1.2 Aliasing

Despite the continuously dark conditions during the polar night, CSTAR light curves are still significantly affected by aliases with periods close to 1 sidereal day. These are due to the daily circular motion of objects around the FoV. This periodic motion can mimic a true signal when combined with slight flat fielding errors. We found these fluctuations were on the order of $0.01 - 0.03$ mag in a light curve depending on the stellar magnitude and position on the detector.

Fortunately, since the period of the alias is known (~ 0.99727 d) we were able to easily identify and remove these features. We phased each light curve on the sidereal day, created a smoothed median template, scaled the power of the signal to match each phase and subtracted the template from the light curve to eliminate contamination from *bona-fide* astrophysical signals. Figure 2.8 shows an example of this alias being removed from a known eclipsing binary *without* distorting the astrophysical variation.

2.3.1.3 Ghosts

The rapid cadence of CSTAR ($20-40$ s) and the long duration of the data stream (nearly 6 uninterrupted months each observing season) allows for the study of stars in an unprecedented fashion. Rare events, such as stellar flares, can be identified and studied in great detail. Qian et al. (2014) showed the modulation of the light curve of a contact binary in the CSTAR field due to the O'Connell effect (O'Connell, 1951) and seemingly aperiodic flaring events throughout the 2010 observing season. Unfortunately, when these flaring events are phased against the sidereal day, they can be traced back to a single 10×10 pixel region on the detector. In fact, upon rigorous inspection, $\sim 20\%$ of 2010 CSTAR light curves exhibit similar features which are likely due to internal reflection or "ghosting" from bright stars (Meng et al., 2013).

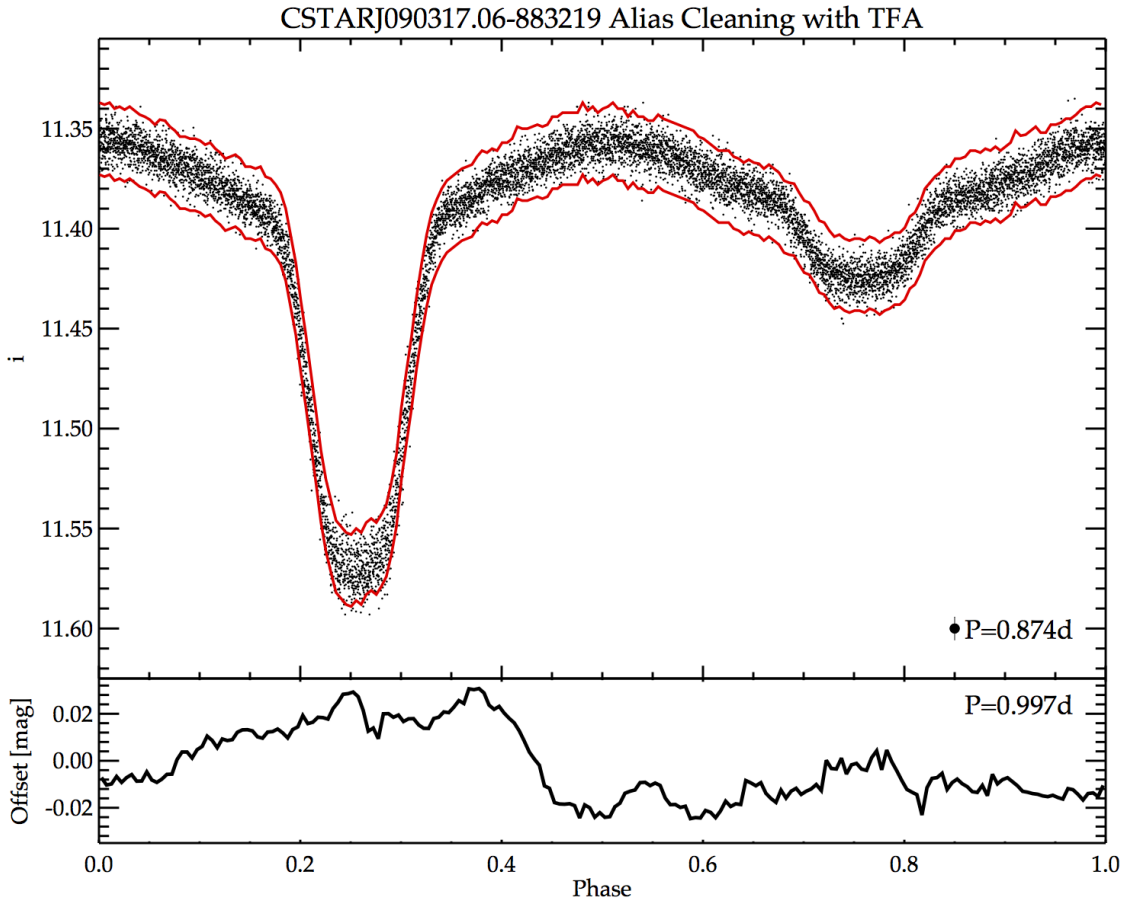

Figure 2.8: Alias Removal
Top: The phase-folded light curve of a known binary CSTARJ090317.06-883219 after alias removal. The light curve has been phased and binned into 10,000 data points. The red lines denote the scatter in the light curve prior to the alias removal. The rms has been decreased by ~ 0.017 mag. The typical photometric error is shown at the bottom right of the panel. *Bottom*: The phase folded aliased signal removed from the light curve. This alias was shown to repeat with a period of the sidereal day.

Figure 2.9 marks the location of the most prominent ghosting features in the CSTAR focal plane and Figure 2.10 shows the eclipsing binary flares from Qian et al. (2014) as impostor signals. It is very likely that fainter ghosts exist given the large number of stars that exhibit "flaring events" which repeat on a sidereal day basis but lie

outside of major tracks.

We first identified these ghosting features when creating the daily transient detection frames. As shown in Figure 2.9, they appear as circles that are not centered on the SCP. As the ghosts have no source in the reference frame, they appear as seemingly moving objects in the differenced frames. It is likely that these signals are caused by the reflections of bright stars both in and near the CSTAR field, as many of these circles appear to track the reflection pattern of a bright star. These ghosts have been found to make changes in a light curve on the order of $0.2 - 3$ mag and last $10 - 45$ min, easily mimicking a flare-like event. Subsequently, any star or transient displaying a flare-like feature had its position checked against these known ghosts and the light curve investigated for similar events occurring at the same point in sidereal phase.

2.3.2 Statistical Fluctuations

The collection of photons on a CCD can be interpreted using Poisson statistics. This is due to the fact each photon hitting the detector in a single exposure is counted independently of the previous photon. In a perfect system, the expected white noise for any given measurement would be $\sqrt{(N)}$ where N is the number of photons counted in the measurement. While this "model" of the noise is sufficient at high photon counts, a more rigorous model must be employed to explain the noise for lower photon counts.

2.3.2.1 Poisson Deviation

The noise in a differenced frame comes from two sources: the science frame and the convolved reference frame. Alard & Lupton (1998) models the effects of noise in a differenced frame building on the typical assumption of $\sigma = \sqrt{I_N}$, where I_N is the photon counts in the frame. The *Poisson deviation* is defined as $\delta = \sqrt{I_N + R_N \otimes K^2}$

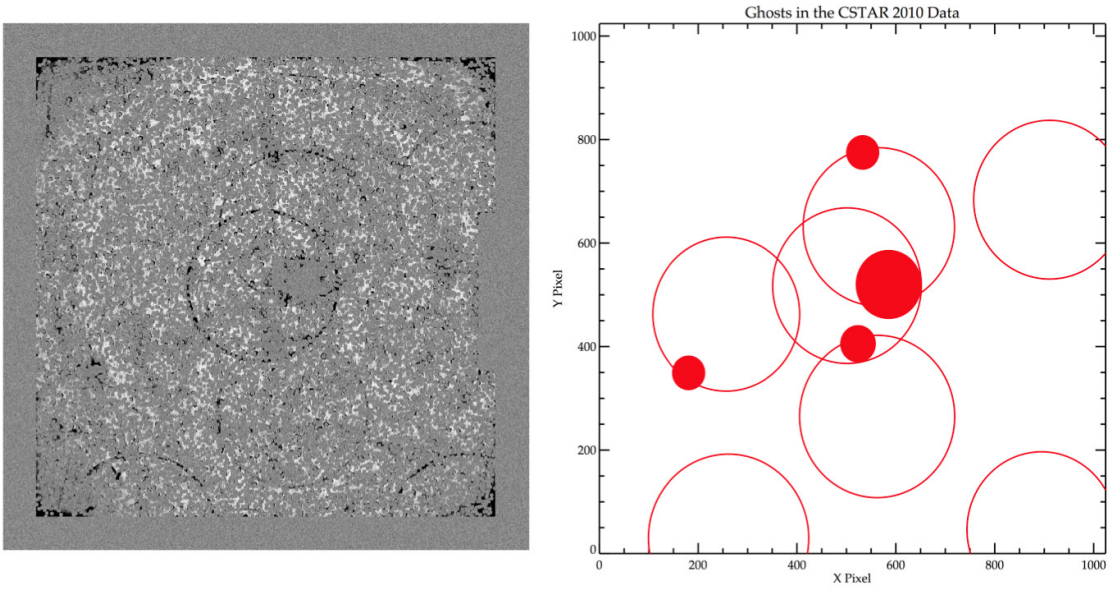

Figure 2.9: Ghost Tracks in CSTAR
The most notable ghosting tracks and saturated stars found in the CSTAR system. *Left*: A 1-day detection frame ($\sim$ 3000 combined images) showing concentric rings not centered on the SCP likely due to ghost reflections. *Right*: The same ghost rings and the sweeping area of diffraction spikes around bright stars (large red dots) are plotted in x-y space of the 2010 master frame.

to describe the effects of the noise in each differenced frame, with R_N being the photon counts from the reference (Alard & Lupton, 1998; Alard, 2000).

Normalizing the pixel values in the differenced frame by δ is a good way to determine if noise is being added by the difference imaging routine. The normalized points should show a Gaussian-like distribution around 0 with a standard deviation close to 1. Figure 2.5 shows the histogram of pixel values for a typical differenced frame normalized by δ. The mean of the residuals is ~ -0.05 with a standard deviation of ~ 1.13. We calculated the χ^2_ν of this differenced frame to be ~ 1.05.

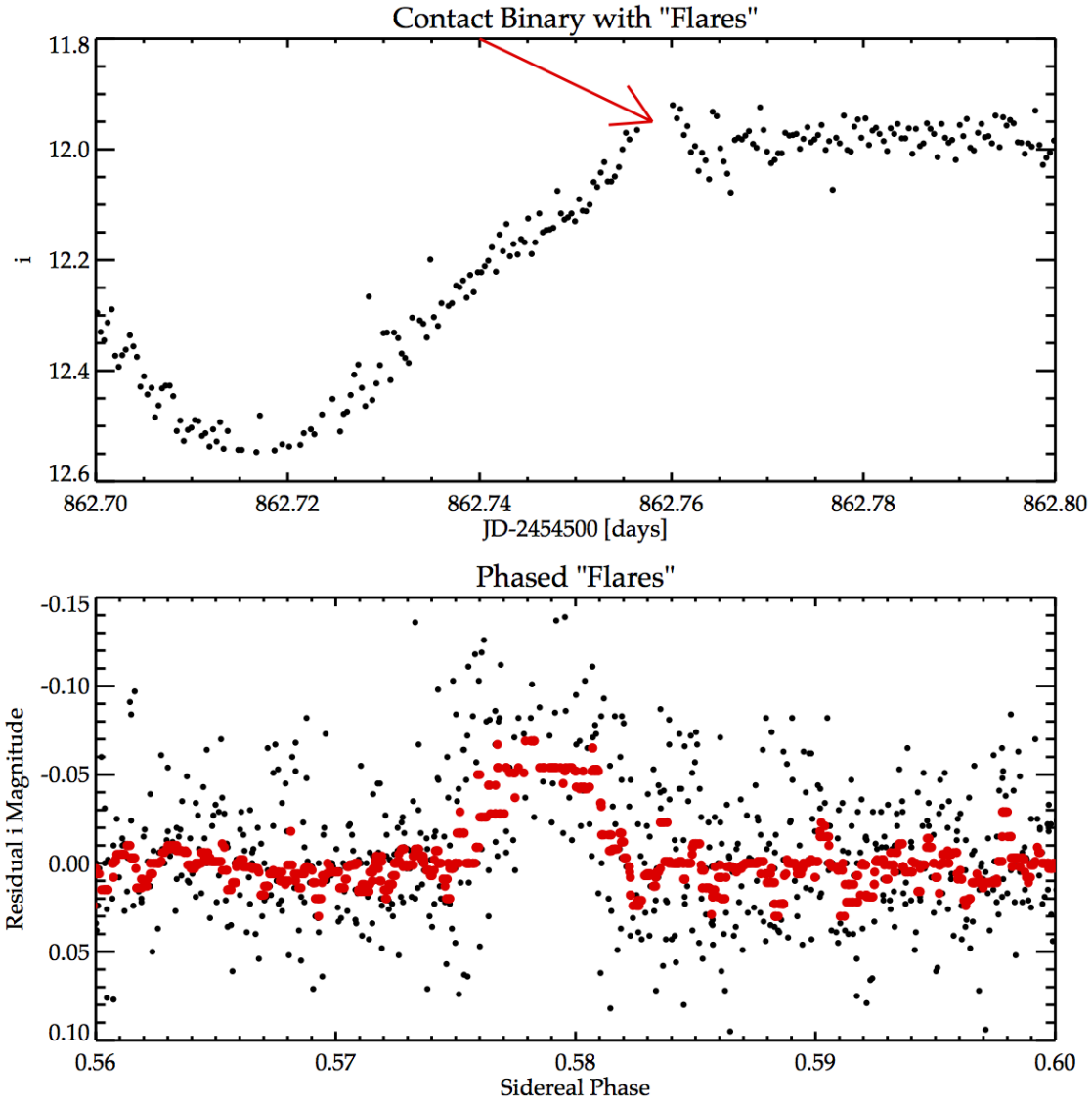

Figure 2.10: Ghost Flares in a Contact Binary

Top: The light curve of the contact binary from Qian et al. (2014) shown to "flare" at different times throughout the 2010 observing season. *Bottom*: The same contact binary plotted in phase space for 1 sidereal day after removing the eclipsing variation. All flares quite obviously line up at the same point in phase, signifying the flaring is occurring across the same set of pixels. The red points denote a smoothed 10-minute median of the phased light curve.

2.3.2.2 Noise Model

Convinced our routine was not adding additional systematics to each frame, we then developed a model for the noise. Astronomical noise from brighter sources is dominated by the number of photons from the source and increases as $\sqrt{I_N}$. This model is the expected dispersion for stars with high photon counts relative to the sky background.

Figure 2.11 shows the change in light curve dispersion with time for stars with g & $r < 8$. Monitoring the change in light curve dispersion over long time intervals (~ 10 minutes) allows us to determine the observing conditions at the site. DIA uses least-squares fitting to match the PSF changes and photometric zeropoint offsets between the reference and science frames caused by clouds and/or changes in airmass. These effects decrease the photon count above the background and increase the photometric dispersion with time. In g, we find bright stars have a dispersion level of < 0.01 mag for 90% of the observing season and < 0.005 mag for 66% of the observing season in 10 minute intervals. In r, we find bright stars have a dispersion level of < 0.01 mag for 72% of the observing season and < 0.005 mag for 23% of the observing season.

The noise for fainter objects is dominated by the sky background, which is present in all 2009 CSTAR images as shown in Figure 2.12. Clear modulation in the levels of the minimum sky background can be seen at a period of 28.8 days due to contamination from the Moon. The step-like nature of the sky background marks the delineation between exposure times of 5 and 20 seconds near MJD 54935.

The noise from the sky is usually modeled as $\pi r^2 I_{\rm sky}$, where r is the pixel radius of the aperture and $I_{\rm sky}$ is the photon counts from the sky in an individual pixel. We can create a complete model for the expected noise in each differenced frame as shown in equation 2.5. The factor of 2 included in the model takes into account the

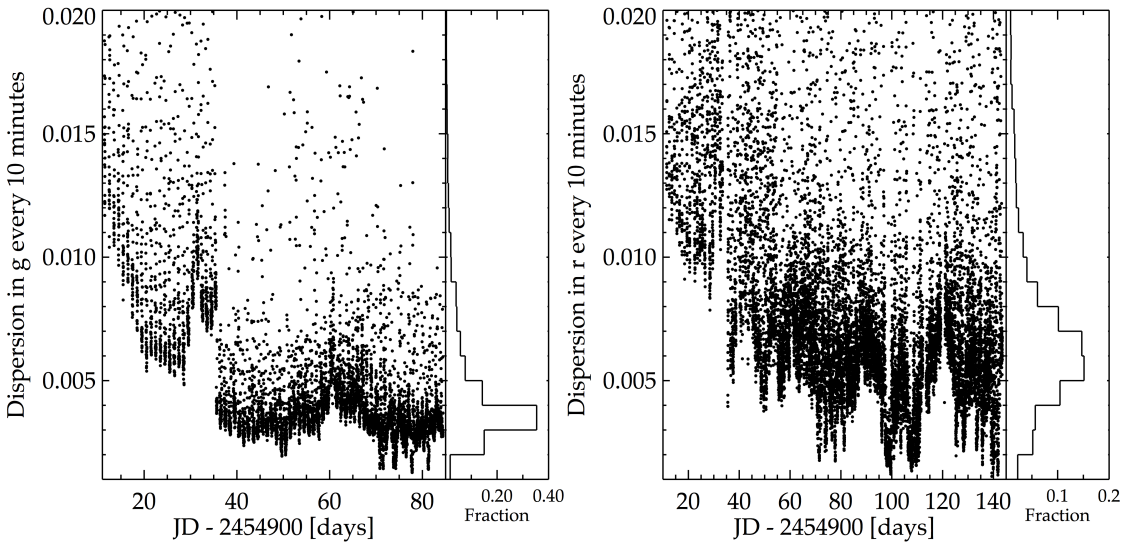

Figure 2.11: Change in Photometric Precision due to Scintillation
The change in photometric precision for 13 bright, non-saturated stars with magnitude < 8 in g & r as a function of Julian date on 10 minute intervals.

additional noise introduced by using a single image for the reference frame instead of a median-combined set of images, due to the reasons described in §2.2.5.1. We then have

$$\sigma = \sqrt{2[I_N + \pi r^2 (I_{sky})]} \tag{2.5}$$

2.3.3 Scintillation Noise

The photometry of bright stars in our sample is constrained by the scintillation limit of the telescope, so we added this feature to our noise model. Young (1967) modeled the effect of scintillation as a function of telescope diameter (d, in cm), altitude (h, in m), airmass (X) and exposure time ($t_{\rm ex}$, in s). We adopt an updated version of this model by Hartman et al. (2005):

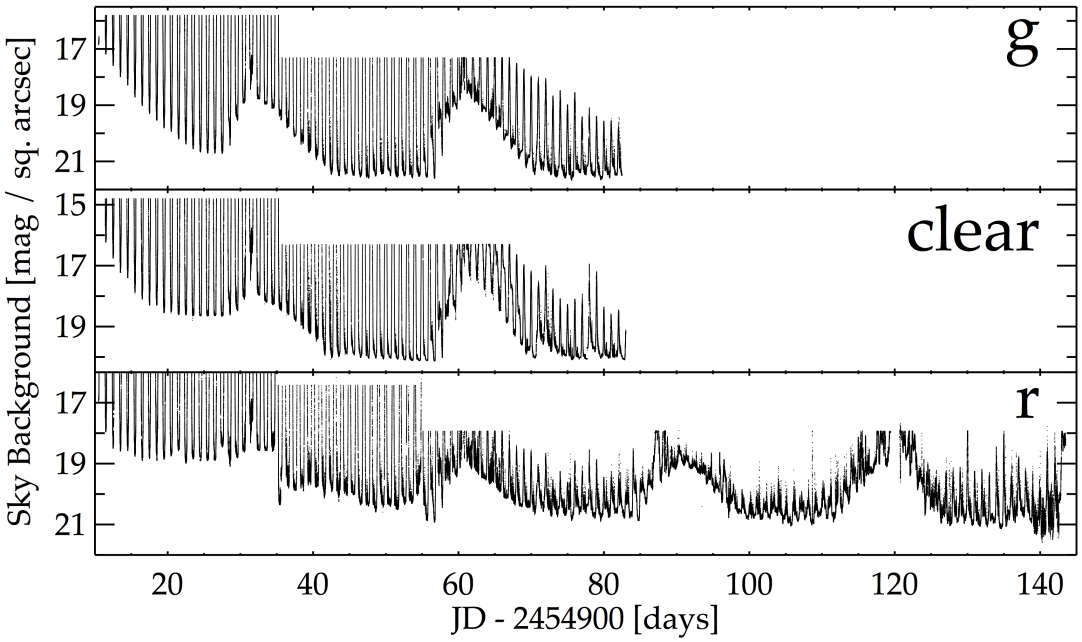

Figure 2.12: Sky Background from Dome A, Antarctica
Sky background in magnitudes per sq. arc second vs Julian date for g (top), *clear* (middle) and r (bottom). The lunar cycle can be seen at JD 2454900 + $\sim$ 30, 60, 90 and 120. The step-like change in the uppermost values of the background is due to a change in exposure time from 5 to 20 seconds.

$$S = S_0 d^{-\frac{2}{3}} X^{\frac{7}{4}} e^{-h/8000} (2t_{\rm ex})^{-\frac{1}{2}} \tag{2.6}$$

where $S_0 \sim 0.1$ (Young, 1967; Hartman et al., 2005). Given the wide FoV of CSTAR, the airmass values of stars in our images are 1.002 ± 0.002. The effective elevation of Dome A is $h = 5100$ m, taking into account the reduced pressure (560mb) due to its polar location. Given a typical exposure time of 20s, we find the scintillation limit to be 1.2 ± 0.1 mmag (with the variation due to the airmass range being considered).

Our final model for the noise and the observed photometric precision in each band is plotted in Figure 2.13. The lowest dispersions were found for stars in the

magnitude range of $\sim 7-10$ in all three bands, where we reached within a factor of 3 of the scintillation noise in g & r. The additional dispersion at $m < 10$ mag in the *clear* data is most likely due to partial and intermittent frosting of the filter. Convinced we were only limited by photon-noise and the scintillation limit we began a search for possible variable stars, transiting exoplanets, binary stars and transient-like events.

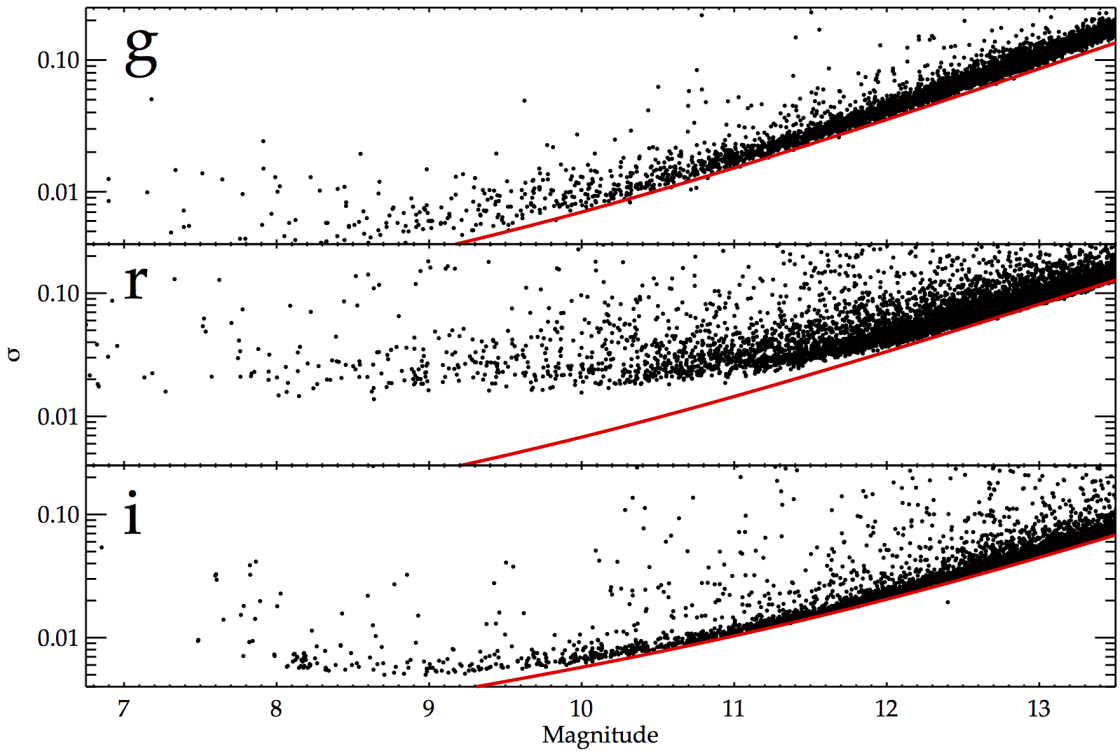

Figure 2.13: Daily Photometric Dispersion
Typical daily dispersions for each band with the expected combined/total error from photon noise, sky noise and scintillation plotted as a red line.

3. SEARCHING FOR VARIABILITY, ECLIPSES, FLARES AND TRANSIENTS*

One of the main goals of this study was to confirm the ability of the DIA code to produce data products precise enough to detect stellar variability even in a hostile photometric environment. If we could prove the code was robust enough to detect low SNR signals then we could be confident in our ability to detect these same signals in highly variable or irregular data. To search for these signals we used a combination of variability and periodicity metrics combined with a slew of variability whitening techniques to remove large amplitude variations which could be masking the eclipses.

3.1 Search for Variability

We employed a combination of 3 variability metrics, following the approach of Wang, L. et al. (2013); Oelkers et al. (2015). First we computed the root-mean-square (hereafter, rms) of all stars and the upper 2σ envelope as a function of magnitude; objects lying above this limit are likely to be genuine astrophysical variables. Next, we computed the magnitude range spanned by 90% of the data points of every light curve (hereafter, Δ_{90}) and its upper 2σ envelope as a function of magnitude. Since we wished that both statistics be based on "constant" stars only and not be biased by large-amplitude variables, both envelopes were calculated in an iterative fashion. We discarded objects located above the median by more than the difference between the median value and the minimum value.

Finally, we computed the Welch-Stetson J variability statistic (hereafter, J (Stet-

*Reprinted in part with permission from "Difference Image Analysis of Defocused Observations with CSTAR" by Oelkers et al., 2015. The Astronomical Journal, Volume 149, 50-63 pp., Copyright 2015 by Ryan J. Oelkers and in part with permission from "Stellar Variability and Flare Rates from Dome A, Antarctica using 2009 and 2010 CSTAR Observations' by Oelkers et al., 2016. The Astronomical Journal, accepted, Copyright 2016 by Ryan J. Oelkers.

son, 1996)) including the necessary rescaling of DAOPHOT errors (Kaluzny et al., 1998). The J statistic is useful to detect variability during short time spans, such as the $5 - 40$ second sampling of the CSTAR data, since it computes the significance of photometric variability between adjacent data points. The J statistic is expected to produce a distribution of values with a mean value close to zero for the "constant" stars and a one-sided tail towards positive values for the "variable" stars. We considered objects lying above the $+3\sigma$ value as variable.

We considered a star to be variable if the star passed all 3 of the above tests in either g, r, *clear* or i. A star was removed from the variable sample if it was within 3.75 (7.5) pixels of a star 2 magnitudes brighter in $i(g\&r)$; the star's *primary* LS period was an aliased period with SNR greater than 1σ of the mean SNR for a given band; or the star had less data than 90% of light curves. The star was returned to the periodic sample if it was later found to have a significant LS period which was *not* an alias. Figure 3.1 shows these techniques recovering the variable candidate CSTARJ192801.90-881331.

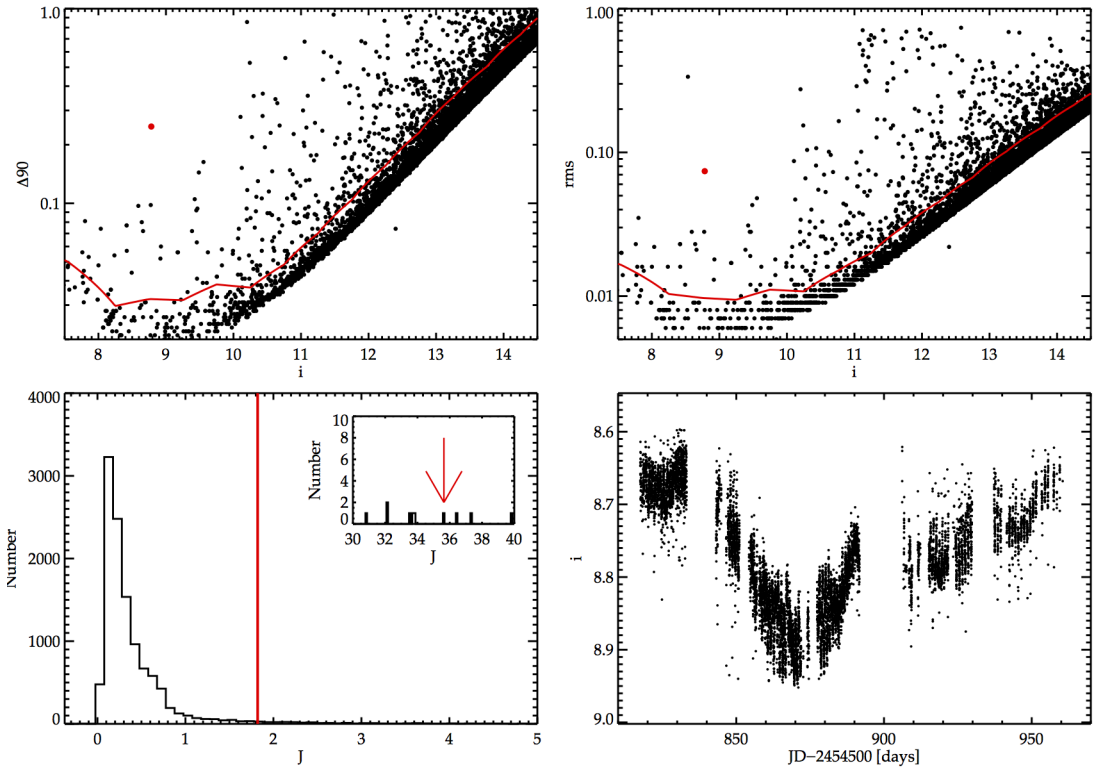

Figure 3.1: Variability Testing

Variability tests used to identify variable candidates in the 2009 & 2010 data sets. Stars lying above the red line in the top panels and to the right of the line in the bottom left panel are expected to be variable. *Top Left*: Δ_{90} statistic with the upper 2σ quartile plotted as a red line. *Top Right*: rms statistic with the upper 2σ quartile plotted as a red line. *Bottom Left*: J Stetson statistic with the upper 3σ cut plotted as a red line. *Bottom Right*: The light curve of the variable candidate CSTARJ192723.13-881334 from the 2010 i data set. The candidate is shown clearly passing each statistic as a red dot in the top two panels and a red arrow in the bottom left panel. The light curve is shown in 10 min bins with the size of each data point being the size of the typical photometric error.

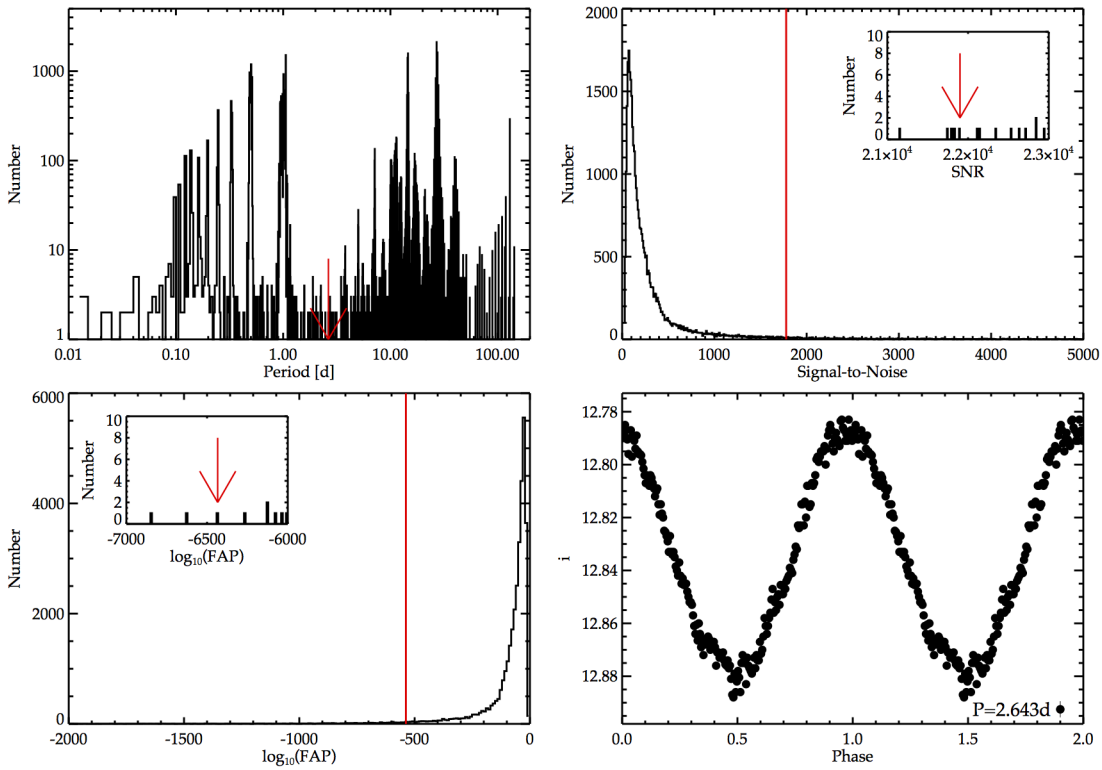

Figure 3.2: Periodicity Testing

The periodicity tests used to identify periodic candidates in the 2009 & 2010 data sets. *Top Left*: the number of "variable" stars with similar periods, indicative of aliasing. The passing candidate is shown with a red arrow. Notice the period is not found on or near a large distribution of other periods; *Top Right*: the $+3\sigma$ cut (red line) on the signal-to-noise ratio. The passing candidate is shown with an arrow; *Bottom Left*: the $+3\sigma$ cut (red line) on the false alarm probability. The passing candidate's $\log_{10}$(FAP) is shown with an arrow; *Bottom Right*: The light curve of a periodic variable star candidate CSTARJ071204.59-875109. The light curve has been phase folded on the recovered period of 2.64 d, binned into 200 data points and plotted twice for clarity. The typical error is shown at the bottom right of the panel.

3.2 Search for Periodicity

We searched each light curve for periodic signals using a Lomb-Scargle periodogram (Lomb, 1976; Scargle, 1982, LS) as implemented in VARTOOLS (Hartman et al., 2008). We computed the 3 highest SNR periods of each star between 0.01 d and the total number of days observed in each band. Each light curve was whitened against the highest SNR period before searching for the next. We checked each signal against known aliases and removed spurious signals. We also applied $+3\sigma$ cuts based on the false alarm probability ($\log_{10}$(FAP)) and SNR. The FAP provides an estimate on the likelihood of a true periodic signal by comparing the SNR of a specific signal to the cumulative distribution of all SNRs. Figure 3.2 shows the technique recovering the period for the candidate CSTARJ071204.59-875109. We removed stars from the periodic sample using the same cuts described in § 3.1.

3.2.1 Search for Transits and Eclipses

We ran the Box Least Squares algorithm (hereafter, BLS) to search for transit- or eclipse-like events which may have eluded our previous variability searches (Kovács et al., 2005). Because the transit is only expected to occur for a very short amount of phase, typically 5% (Charbonneau et al., 2000), the signal is non-sinusoidal. The BLS routine searches for signals caused by a periodic alternation between two flux levels, H (the out-of-transit level) and L (the transit level). By searching the over the parameter space of period, eclipse depth and transit length the probability of detection for a small, periodic, eclipse-like feature is greatly increased.

Prior to each eclipse search we pre-whitened the light curve against the primary LS period and its 10(9) (sub-)harmonics. We then searched each light curve for transits with periods between 0.1 d and a third of the maximum observing length (to ensure a minimum of 3 transits) with a transit length of 0.01 and 0.1 of the period.

We allowed for 10,000 trial periods and 200 phase bins. We also adopted a number of detection thresholds that are common among exoplanet searches. We required no less that 3 transit events for every candidate to ensure no significant variation between the odd and even eclipses, which would suggest an eclipsing binary over a transit. While typical planetary transits produce a drop in the light curve of only 1 to 2%, we kept larger depth events since they could be due to other interesting objects such as brown dwarfs or eclipsing binary stars. We then subjected each light curve to criteria based on the statistics of the BLS routine.

Typically, the error in ground based milli-magnitude photometry is correlated. Because this is the regime we will be searching for exoplanets, we will investigate the S_{red} statistic described in Pont et al. (2006) to determine the significance level of each transit. Any transit candidate with a S_{red} statistic greater than 7 will be considered significant. True transits will only show the systematic dimming of each light curve and not a systematic brightening or anti-transit. Burke et al. (2006) suggests a transit to anti-transit statistic $\Delta\chi^2/\Delta\chi^2_-$, where both the transit and anti transit χ^2 are compared. Only stars with the statistic > 1.5 are considered candidates.

3.3 Search for Stellar Flares

We searched for flare events using the IDL function GAUSSFIT with a 6-term solution to allow for symmetric and asymmetric flare detection. Similar to the BLS search, we pre-whitened all light curves against the most significant LS period and its 10(9) (sub)harmonics. Each whitened light curve was broken into 0.25 d bins with at least 50 data points per bin prior to the fit. Any best-fit gaussian with $0.8 < \chi^2_\nu < 1.2$ and a flare amplitude greater than the rms of the light curve passed the first significance cut.

All passing events were phased on the sidereal day to check against "ghosting"

signals. Any recurrent event in sidereal phase was flagged as a spurious “ghost" detection. This procedure was repeated, phasing the events on the whitened LS period to identify events which may have been artifacts of the whitening process. Similarly, the MJD of each flare was checked against all other flare event timings to rule out events which were caused by global artifacts, such as misalignments or bad subtractions. The phase of each flare event was also visually inspected to confirm there were no other noticeable flares, indicative of ghost events and the previous and next sidereal day were examined to ensure no similar variation occurred. Additionally, any star with a candidate flare in g or r observed between MJD 54955-985, when the observations overlapped, had its light curve inspected in the alternate band. If the flare did not pass the cuts mentioned above then it was removed from the candidate list.

Any flare timing within 5 min of a flare in *another* star was flagged and removed. The position of each flaring star was required to be more than 5 pixels from a known ghosting track or bleed trail from a saturated star. Candidates were further constrained to have $0.95 < \chi^2_\nu < 1.05$ to remove candidates which were fitting the noise of a light curve instead of flare-like variation. Lastly, we removed stars from our flaring sample which did not pass the cuts for proximity or aliasing mentioned in § 3.1.

We attempted to quantify the possible ghost contamination in our sample because of the large number of light curves showing ghosting events. We estimated this contamination by injecting fake flares of varying amplitude, length and phase into simulated light curves with varying noise. These contaminated light curves were then run through our selection process. We found on average 12% of the total flares recovered were ghost contaminants with lengths < 45 min. We use this contamination rate to correct our flaring fraction.

To quantify the flare rate and make comparisons to the previously mentioned studies we needed to select the stars which were the most likely to be K/M dwarfs. We identified the stars in our data set using the 2MASS catalogue (Skrutskie et al., 2006) to provide *JHK* magnitudes. We combined the *J-H* vs. *H-K* color-color diagram with the stellar locus for K5V-M9V provided by Pecaut & Mamajek (2013). We selected stars with 2MASS photometric errors $\sigma < 0.2$ mag and within $\pm 1\sigma$ of the *J-H* vs. *H-K* locus as the most likely dwarf candidate members. To estimate contamination by background giants we queried the TriLegal model (Girardi et al., 2012) for the Galaxy and applied the same cuts. We estimate our contamination to be $< 1\%$ at each spectral type. We estimate the Galactic reddening vector with the relations from Fitzpatrick (1999) and find extinction would preferentially scatter early type dwarfs into our selection sample. However, since E(B-V) at the SCP is ~ 0.16 mag Schlafly & Finkbeiner (2011), the expected color excess in the 2MASS bands is E(J-H)< 0.05 mag and E(H-K) < 0.03 mag. We expect these effects to cause minimal contamination from early-type stars.

3.4 Search for Transient Events

DIA provides a unique opportunity to detect variability in a star field before searching through light curves, since correlated residuals on a differenced frame indicate a statistically significant change in flux. A "detection" frame can be created by co-adding the absolute values of differenced frames to achieve a higher SNR identification of variable or transient behavior. Each differenced frame was normalized on a per-pixel basis by the square root of the sum of the counts in the science and reference frames before the co-addition. We also masked all pixels within a 5-pixel radius of the position of any point source in the master list.

Due to the nearly-polar location of Dome A, many images were contaminated by

satellite tracks which were masked as follows. The FIND routine was used to identify sources in each differenced frame with stellar-like PSFs. These objects were temporarily masked and a line was fit to any remaining pixels with large positive deviations ($> 10\sigma$ above the mean background) using the IDL routine ROBUST_LINFIT. If the residuals of the fit had a standard deviation < 3 pix, a trapezoidal mask was placed along the best-fit line. This process was repeated until no best-fit line was found to account for multiple satellite trails. The temporary masks were then removed and the absolute value of the frame was taken. The final detection frames were made by co-adding all frames obtained within a 24 hour window (typically > 3200 frames).

The detection frames were inspected for correlated residuals with stellar-like PSFs in the "blank" areas of the master frame. Recall that all point sources detected in the master frame were masked in these detection frames; therefore this search was specifically aimed at identifying transients arising from objects normally lying below the limiting magnitude of CSTAR. 7×7 pixel stamps centered on each transient candidate were extracted and retained if they exhibited a $> +5\sigma$ variation above the sky background. If a transient event occurred in g & r between MJD 54955-985 its position and timing were checked in the alternate band to aid in confirmation. Any transient without a counterpart was removed from our sample.

Fluxes were then extracted from all differenced frames (as described in § 2.2.6) for two reasons. The first was to check for *bona-fide* variation of the transient light curve, which might have been missed by the metric above. The second was to give a robust sample of possible aliasing flares described in § 2.3.1.3. Since the majority of each transient light curve was simply the sky background, variations due to moonlight or twilight had to be removed by subtracting the median sky value of the image from each transient light curve.

Each transient candidate light curve was checked against known aliasing features

as follows. The light curve was divided into segments spanning 0.01 sidereal days and the mean magnitude of each fragment was compared to $\bar{m}_\phi$, defined as the mean magnitude of all other sections of the light curve spanning the same fractional sidereal day during the rest of the season. The variation was considered *bona-fide* if it contained at least 10 data points and lay $> +2\sigma$ above $\bar{m}_\phi$. The timing of each transient passing these cuts was further checked against the timing of *all* others. If an event was found to coincide in time with another candidate, both were discarded as spurious.

3.5 Results

3.5.1 Variability and Periodicity Searches

Previous studies of CSTAR data (Wang, L. et al., 2011, 2013; Oelkers et al., 2015; Yang et al., 2015) have generated lists of variables by applying a binary classification (i.e., an object is either variable or not, based on a set of criteria). In this work, we present the likelihood of variability and/or periodicity for every object, computed as follows. Stars meeting the variability criteria in g or r received one point per band, while two points were awarded for i because those images were in focus and well sampled. Similarly, stars exhibiting a significant periodicity received 2 points in i and 1 in g & r. We found 45 objects to have a variability or periodicity (LS or BLS) score of 3 or more, signifying a high likelihood of variability. Table 2.1 is an example list of all stars in our sample and their resulting scores which will be included with the stellar library. If the star had a variability or periodicity score of 3 or more, its type was estimated in Table 2.1.

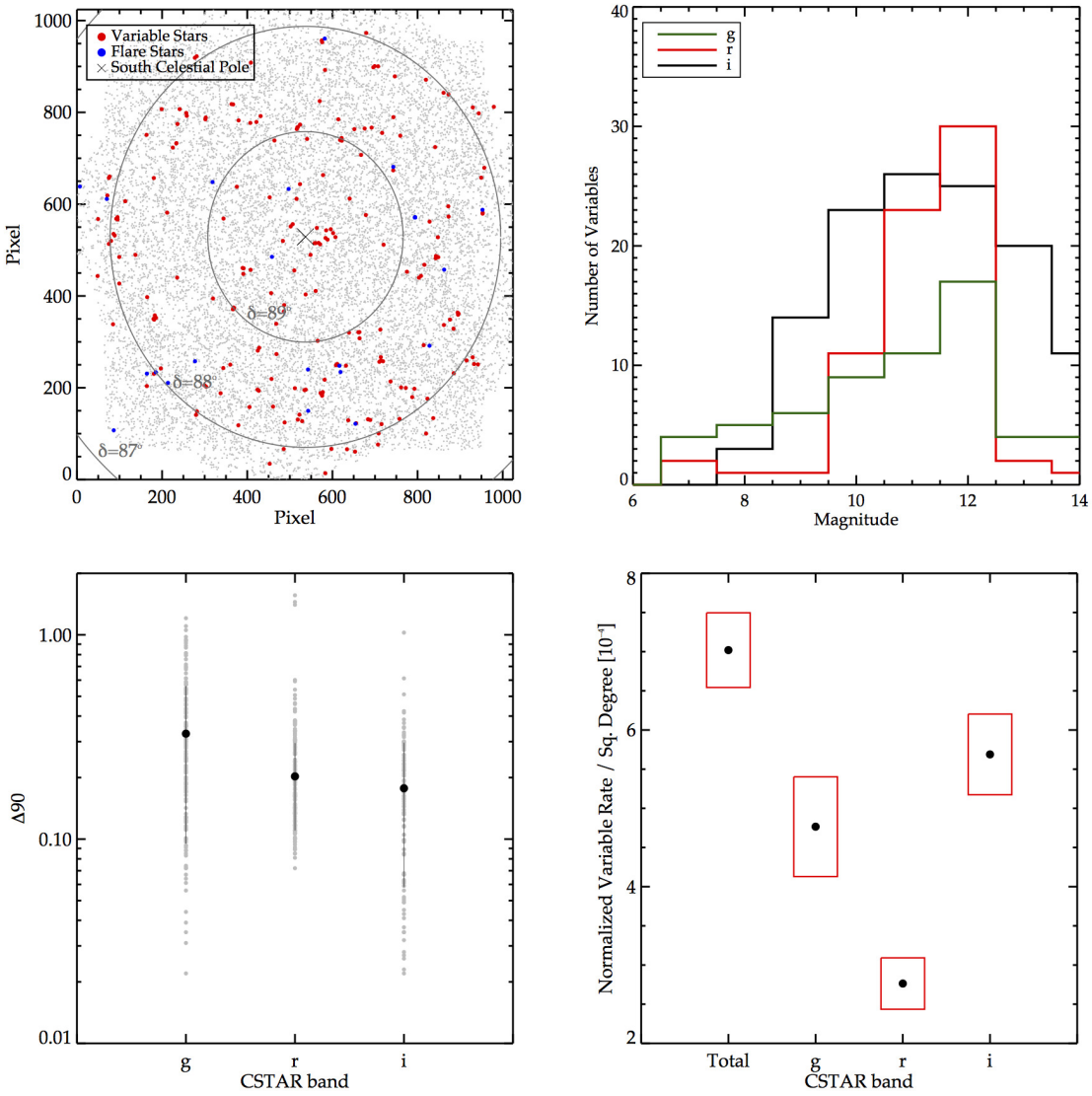

Figure 3.3: Variability Rates with CSTAR

Top Left: Positions (in CSTAR detector coordinates) of stars in our library (grey dots). Catalogued variable stars are shown with red dots; flaring stars are shown with blue dots; the cross marks the SCP. The points appear to be randomly distributed across the detector. *Top Right*: The number of variable stars identified as a function of magnitude for a given band. *Bottom Left*: The Δ_{90} statistic for all identified variable stars in a given band. Variability appears to be large in *g*. *Bottom Right*: The normalized variable star rate for a given sq. degree of the sky. All errors are based on Poisson statistics and agree with previous reductions of the CSTAR data sets.

Numerous reductions of the CSTAR data sets have identified many new and intriguing variable stars. The unprecedented cadence of the telescope over a 6-month period allows for a statistical analysis of the number of variable stars which could be visible in a given FoV. Figure 3.3 shows all of the variable stars in our field as well as the flaring stars described below. We find the majority of our recovered variable stars are mag$\sim$ 12 in all bands with variables in g showing the largest magnitude variation. Finally we determined a normalized variable rate of $7.0 \pm 0.5 \times 10^{-4}$ variable stars per sq. degree across all bands, $4.8 \pm 0.6 \times 10^{-4}$ for g, $2.8 \pm 0.3 \times 10^{-4}$ for r and $5.7 \pm 0.5 \times 10^{-4}$ for i. These rates are consistent with previous studies of the CSTAR field.

A specific advantage of the 2009 CSTAR dataset is the addition of 3-color photometry. Variable stars in the CSTAR field now have the unique opportunity to be studied for variations in both time and color. Figure 3.4 is a color - color diagram for stars in our sample with *gri* magnitudes. We find $\sim 91\%$ of the stars in our sample have $g-r > 0$. This is consistent with the CSTAR field being directed towards the galactic halo and confirms previous and current variable star searches in the field finding many irregular and multi-periodic RGB or AGB-like stars. Indeed we find normal pulsators, such as RR Lyraes or δ Scuti stars, multi-periodic and irregular variables have $\langle g-r \rangle \sim 0.59$. In contrast the eclipsing binaries, which are expected to have a wide variety of ages along the main sequence, have $\langle g-r \rangle \sim 0.22$.

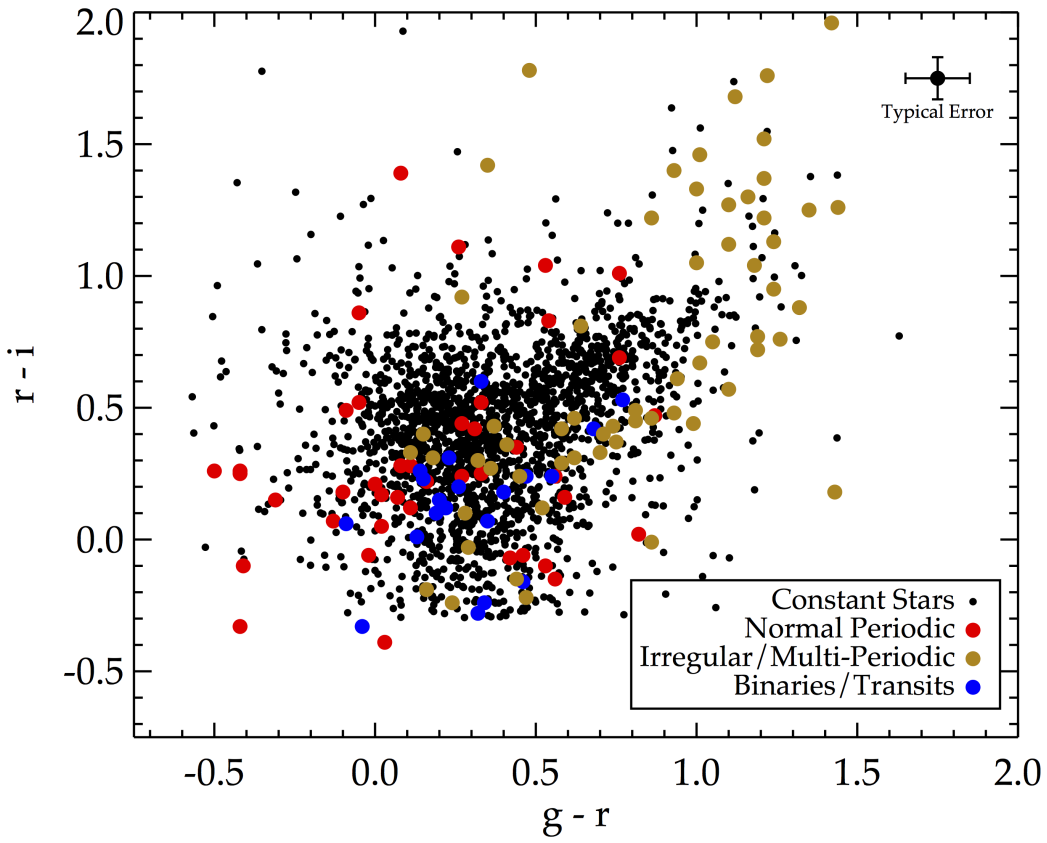

Figure 3.4: Color-Color Diagram of Stars in 2009 CSTAR Library
Color-color diagram for stars in our 2009 CSTAR sample with three-band photometry (the i-band data is from the 2010 CSTAR photometry of Wang, L. et al. (2013)). Small black points denote the data points constant stars. Red points are regular periodic variables such as RR Lyrae, δ Scuti and γ Doradus. Gold points are irregular, multi-periodic and long-term variable stars. Blue points are eclipsing binaries.

The defocused nature of the observations likely aided in the identification of 7 stars as variable. These stars were either close to or fully saturated in the i data from 2008 and 2010. The American Association of Variable Star Observers (AAVSO) has previously catalogued 4 of these stars. The AAVSO has classified 2 of these

variables, #p09-004 and #p09-002, as a slowly-varying and a non-periodic semi-regular variable, respectively. After our LS search we found both of these stars to have periods passing our threshold criterion of 60.5 d and 22.2 d respectively. #p09-003 is archived in the AAVSO database as a miscellaneous variable with a period of 73.3 d. We found this variable to be semi-regular, currently exhibiting a main period of 16.6 d. We have also recovered the variability in #p09-007, which is classified as a δ Scuti star with a period of 0.12 d.

Figure 3.5 shows the light curves of 9 variable stars in our 2009 data set. #p09-007 is an example of a bright star ($g \sim r \sim 6.8$ mag) that was saturated in CSTAR observations carried out during other winter seasons when the array was in focus. The defocused nature of our images allowed it to remain below the saturation limit, enabling a period determination of 0.122 d. Previous studies of #n106372 classified this star with a period of 12.5 d (Wang, L. et al., 2011). We recover the star as periodic but with a significant period of 0.57 d in all bands. The remaining variables shown in the Figure 3.5 were present in the 2008 and 2010 data sets and span a variety of types and periods.

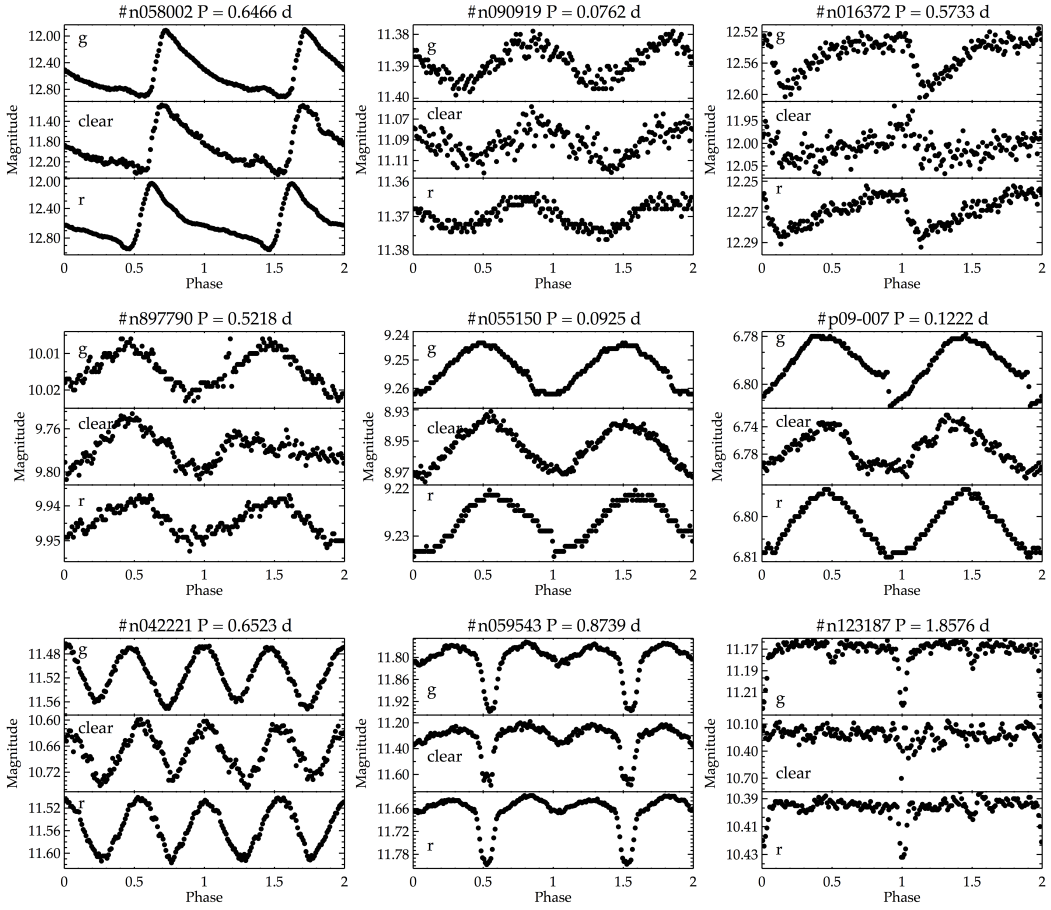

Figure 3.5: Recovered Variables

Light curves for 9 variable stars in g (top), *clear* (middle) and r (bottom) showcasing the different types of objects present in our sample (from top left to bottom right): RR Lyrae (#n058002); periodic variable (#n090919); periodic variable (#n106372); γ Doradus (#n897790); periodic variable (#n055150); δ Scuti (#p09-007); contact binary (#n042221); semi-detached binary (#n059543); and detached binary (#n123187). The light curves have been phased and binned into 200 data points.

Numerous reductions of the CSTAR data sets have identified many new and intriguing variable stars. The unprecedented cadence of the telescope over a 6-month period allows for small-scale variation to be robustly detected. Figure 3.6 shows the

g and r light curves of #n057725. This variable exhibited very regular, Cepheid-like pulsations in the 2008 i data and a much more complex light curve structure in the 2010 i data, with clear evidence of eclipses. The 2009 light curves show enhanced variability in the cepheid-like modulation of the light curve. The expected times of eclipse are highlighted with red arrows for primary eclipses and blue arrows for secondary eclipses. We applied a smoothing kernel to the light curves to aid in the recovery of the suspected binary eclipses. We find we recover both the primary and secondary eclipses in g & r at the expected eclipse times.

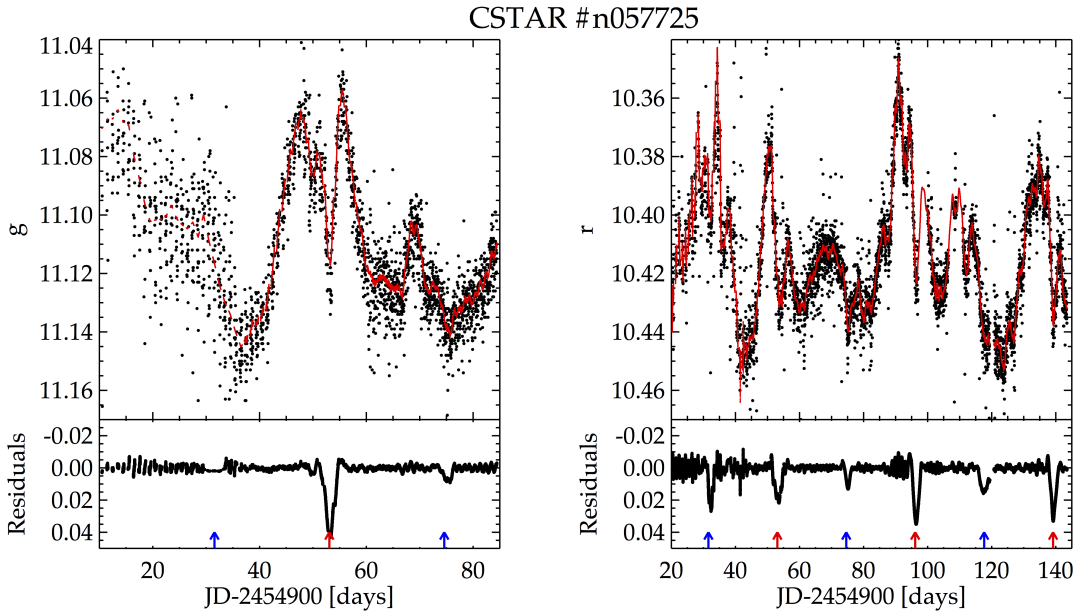

Figure 3.6: Population II Cepheid in an Eclipsing Binary System
Light curves of #n057725, a likely Population II Cepheid in an eclipsing binary system showing complex variability. The top panels show the 2009 g and r light curves with the smoothed light curve over-plotted. The bottom panels highlight the eclipse-like events that take place every 43.2 d. Red arrows mark the expected time of primary eclipse and blue arrows mark the expected time of secondary eclipse.

Table 3.1: Candidate Flares in 2009 and 2010 CSTAR Data

CSTAR ID	R.A.	Dec.	Filter	K/M Dwarf	MJD-2454500	Length [d]	Amplitude [mag]	Comment
CSTARJ111143.79-875135	11:11:43.79	-87:51:35	i	K5V	887.181580	0.350	0.027	...
CSTARJ100426.56-883937	10:04:26.56	-88:39:37	i	...	881.362122	0.065	0.016	...
CSTARJ104851.25-882931	10:48:51.25	-88:29:31	i	...	859.818665	0.102	0.096	...
CSTARJ112329.83-891523	11:23:29.83	-89:15:23	i	...	858.012878	0.022	0.336	...
CSTARJ150830.36-885721	15:08:30.36	-88:57:21	i	...	832.369446	0.324	0.015	...
CSTARJ115040.50-892747	11:50:40.50	-89:27:47	i	K6V	827.375916	0.777	0.014	...
CSTARJ064616.70-874825	06:46:16.70	-87:48:25	i	...	847.265564	0.023	0.298	...
CSTARJ062327.70-875637	06:23:27.70	-87:56:37	i	...	886.023499	0.310	0.057	...
CSTARJ210848.50-892830	21:08:48.50	-89:28:30	i	...	865.311279	0.022	0.574	...
CSTARJ034834.23-882808	03:48:34.23	-88:28:08	i	...	861.093262	0.490	0.045	...
CSTARJ021530.10-873840	02:15:30.10	-87:38:40	g	...	468.947968	0.028	0.081	drop out in r
CSTARJ054239.09-872933	05:42:39.09	-87:29:33	g	...	476.092010	0.270	0.033	drop out in r
CSTARJ100426.56-883937	10:04:26.56	-88:39:37	g	...	478.015503	0.033	0.032	drop out in r
CSTARJ153412.75-881014	15:34:12.75	-88:10:14	g	...	472.540314	0.260	0.260	seen in r
CSTARJ060139.40-880138	06:01:39.40	-88:01:38	g	...	481.687744	0.410	0.049	no star in r
CSTARJ060745.20-882219	06:07:45.20	-88:22:19	g	M2V	479.106659	0.032	0.031	drop out in r
CSTARJ203720.10-880633	20:37:20.10	-88:06:33	g	...	471.879669	0.120	0.034	drop out in r
CSTARJ172731.23-885235	17:27:31.23	-88:52:35	g	M8V	477.950073	0.140	0.018	drop out in r
CSTARJ122630.23-882031	12:26:30.23	-88:20:31	g	...	449.685028	0.248	0.665	outside window
CSTARJ100731.56-884333	10:07:31.56	-88:43:33	g	...	471.660156	0.230	0.320	drop out in r
CSTARJ100737.56-880919	10:07:37.56	-88:09:19	r	...	506.169220	0.120	0.045	outside window
CSTARJ090621.10-882040	09:06:21.10	-88:20:40	r	M0V	490.181580	0.230	0.219	outside window
CSTARJ042931.75-893647	04:29:31.75	-89:36:47	r	...	481.773285	0.151	0.779	no star in g
CSTARJ010728.36-885510	01:07:28.36	-88:55:10	r	...	534.605530	0.215	0.151	outside window
CSTARJ022220.06-875619	02:22:20.06	-87:56:19	r	...	485.373688	0.290	0.283	outside window
CSTARJ053807.80-875538	05:38:07.80	-87:55:38	r	...	506.498016	0.370	0.389	outside window
CSTARJ090738.25-884334	09:07:38.25	-88:43:34	r	...	527.660156	0.076	0.564	outside window
CSTARJ210122.50-874600	21:01:22.50	-87:46:00	r	...	531.661865	0.320	0.162	outside window
CSTARJ141243.70-883232	14:12:43.70	-88:32:32	r	M7V	506.367676	0.399	0.154	outside window

3.5.2 Flare Search

We identified 10, 10 and 9 flare events in *i, g* & *r*, respectively leading to a total of 29 flares throughout the nearly 3000 combined hours of observations between 2009 and 2010. This leads to a total flaring rate for the entire CSTAR field of $7 \pm 1 \times 10^{-7}$ flares/hr. Details for each flare event are shown in Table 3.1 and Figure 3.7 shows light curves of 9 events of varying amplitude and length. Of the stars which could have been visible in both *g* & *r* we found only one object. The remaining events either did not have a counterpart in the other band, took place at a time where no data was available in the other band or experienced a data drop out at the time of the flare.

The normalized flare rates for the searched spectral types, K5V-M9V, are $5 \pm 4 \times 10^{-7}$ flares/hr (Late K) and $2 \pm 1 \times 10^{-6}$ flares/hr (M) as shown in Fig 3.8. All other stars in our sample were shown to flare at a rate of $6 \pm 1 \times 10^{-7}$ flares/hr. We found 6 stars in this spectral range to flare, which is consistent with our expectations of $1 - 4$ flaring K/M dwarfs from the previously-defined flaring fraction. These rates are in contention with previous studies of the flare rates for these spectral types, $\approx 4 \times 10^{-4} - 10^{-1}$ flares/hr (Davenport et al., 2012; Hawley et al., 2014). These rates were shown to be highly dependent on the activity level of the star.

We hypothesize our flare rates are lower because of a combination of factors. First, the relative age of stars in the halo is typically older than that of stars in the disk (Jofré & Weiss, 2011). Kowalski et al. (2009) showed the flare rate was highly dependent on galactic latitude. As the CSTAR field is centered at ($l \approx 303$, $b \approx -27^{\circ}$) it is dominated by halo stars (Wang, L. et al., 2013; Oelkers et al., 2015). Studies of stellar rotation and activity relations for diverse stellar ages have shown older stars decrease their magnetic activity as they age (García et al., 2014).

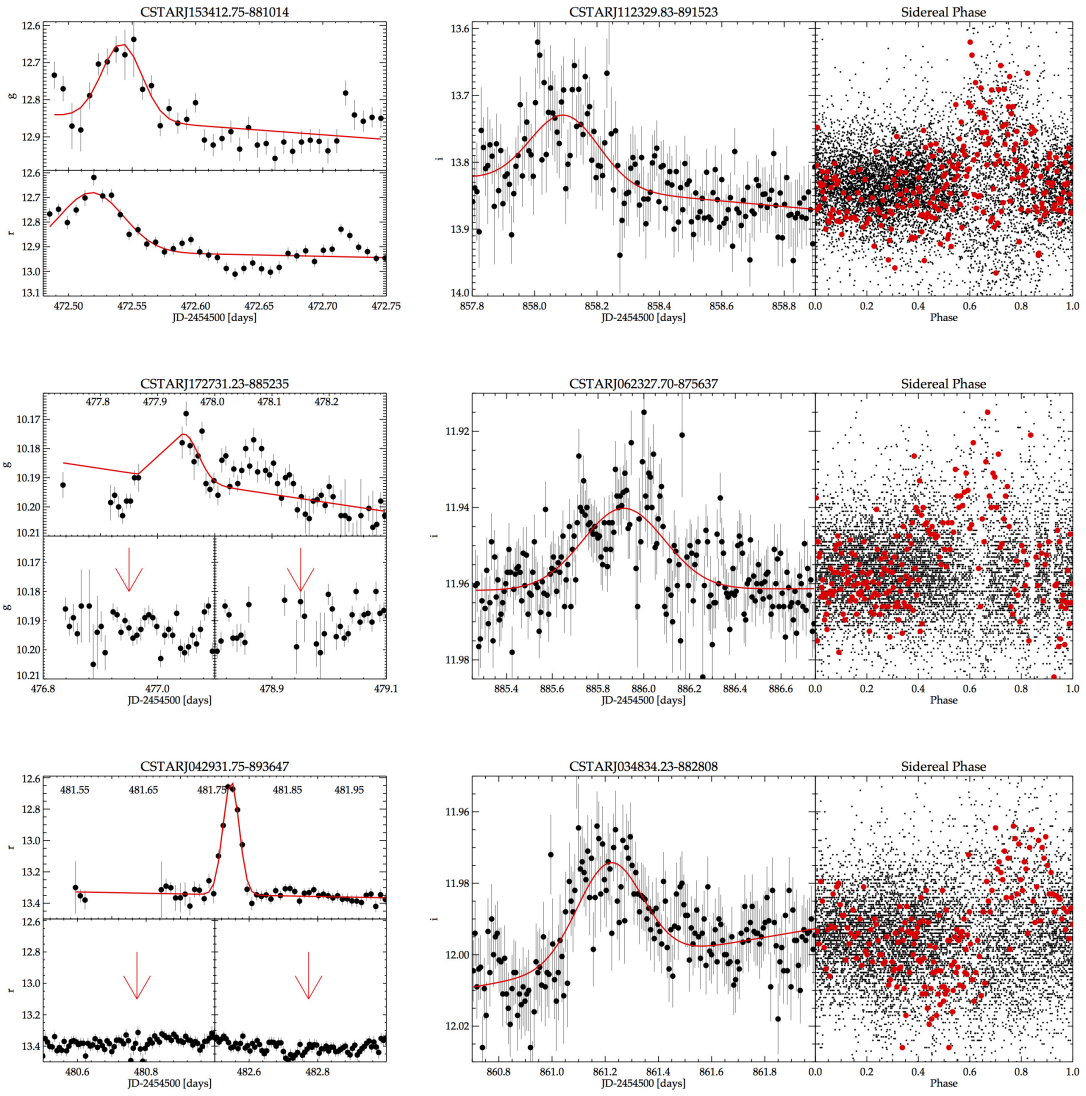

Figure 3.7: Flare Candidates

Light curves of 9 flaring events, with various lengths and amplitudes, all flagged as genuine in our search. Each panel shows a particular technique to remove ghost contamination. *Top Left*: The flare appears in both *g* & *r*. *Bottom and Middle Left*: The flare does not occur in the previous or next sidereal day, suggesting a genuine event. *Right*: The flares do not appear to coincide with any noticeable features when phased on the sidereal day. Red points in the phase-folded light curve denote all photometric points visible in the left panel. All light curves have been binned in 10-minute intervals.

Therefore an older, magnetically inactive halo population would flare at a lower rate than a more diversely aged population as is found in the disk (i.e. stars in the Kepler field (Hawley et al., 2014)). Similarly, Hawley et al. (2014) showed inactive M-dwarfs could have flare rates lower than active M-dwarfs by 2-3 orders of magnitude.

Finally, a major contributing factor to our lower flare rate is that we are biased against detecting *all* flares due to the rampant ghosting events in the CSTAR data sets. Many of the flares contributing to the flare rates in previous work were found with significantly more precise photometry, from the Kepler space telescope, and had durations < 1 hr, a timescale identical to ghost reflections (Hawley et al., 2014; Davenport et al., 2014; Lurie et al., 2015). We corrected our flaring rate for ghost contamination by subtracting our expected contamination rate for flares with timescales less than 45 minutes as determined in § 3.3 but because we made many cuts on simultaneous events, sidereal phase timing and flare duration we likely removed *bona-fide* flares from our sample. If the telescope had returned more simultaneous, multi-band data during the 2009 or 2010 seasons we would be able to better constrain, identify and categorize more flare candidates.

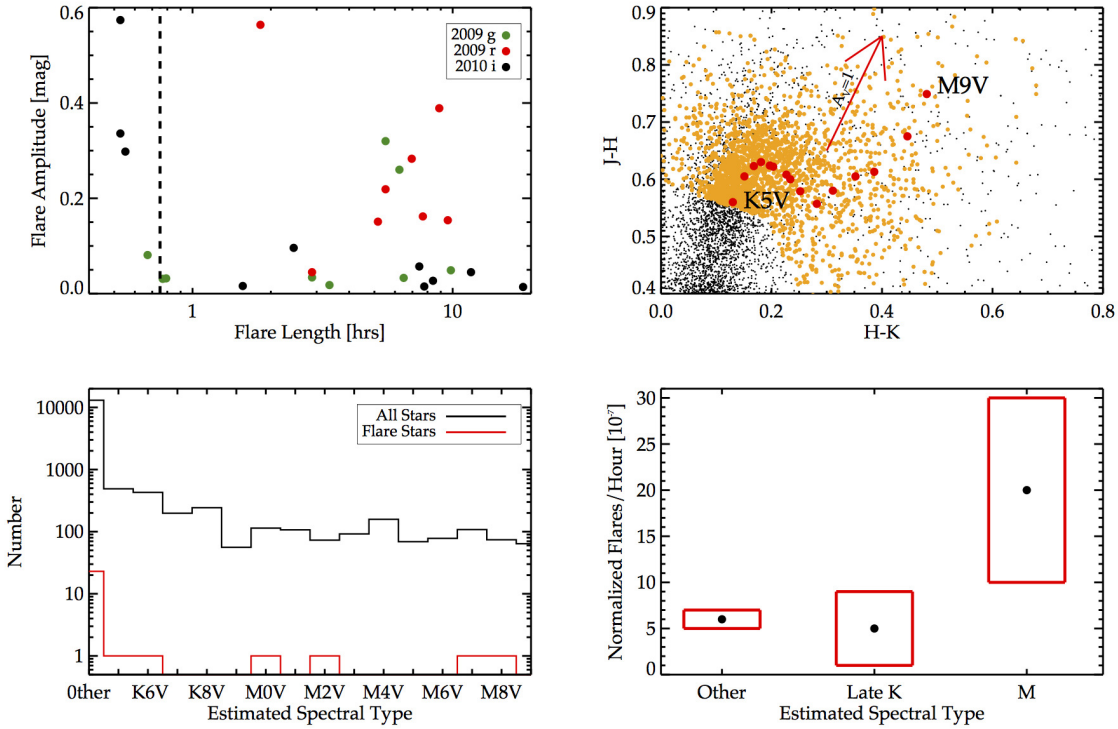

Figure 3.8: Flare Rates with CSTAR

Top Left: Flare timing vs. flare amplitude for all events flagged as genuine. The dashed line shows the maximum length of ghosting events. Any event to the right of this line is likely to *not* be a contaminating ghost. *Top Right*: Selection of dwarf stars using 2MASS J-H vs H-K colors and the stellar locus of Pecaut & Mamajek (2013). Stars with 2MASS colors falling within 1σ of a stellar loci and with 2MASS photometric error < 0.2 mag were selected as dwarf candidates. The reddening vector shown is based on the extinction law from Fitzpatrick (1999). *Bottom Left*: Histograms for the total number of late K and M dwarfs in the CSTAR data set. The red histogram shows flaring stars in our sample. *Bottom Right*: Normalized flare rates derived from our observations and errors are based on Poisson statistics. All results are consistent given their uncertainties.

3.5.3 Transient Search

We identified 331, 53 and 15 possible transient events in *i, g* and *r*, respectively. However, throughout our analysis it became quite clear many systematic effects can mimic transients, specially at low flux levels. After studying the timing of each event as well as its duration and amplitude, it became clear that *none* of the candidates could be distinguished from known detector systematics. Many identified transients either showed no variation in their light curve at the expected time or exhibited signals which mimicked those found in § 2.3.1.3 at nearly the same fractional sidereal day ($\pm$ 0.01). Other transients occurred only once during the season, but were found to occur at the same time as other events elsewhere in the focal plane. Figure 3.9 shows examples of such impostors. While no events were identified, our null result is consistent with the probability of a supernova being less than 2% based on CSTAR's limiting magnitude and FoV.

We find the design of CSTAR may not have been well suited for blind transient searches due to the large pixel scale ($\sim 15''$) and lack of a tracking mechanism. The large pixel scale forced many sources into the same pixel. The pixel scale also exacerbated the difficulty of locating the source of the transient event in a possible $1.25'$ radius. The large pixel scale also created a shallow limiting magnitude (13.5 in $g\&r$ and 14.5 in i) which greatly reduced the telescope's ability to detect Galactic and extragalactic transients. Furthermore, the lack of a tracking mechanism increased the number of sources affected by ghosting events. We find these events to be so common and wide spread that if a short-duration transient event were to be detected with no other known counterpart it is more likely the event is caused by an asymmetric reflection than truly being astrophysical in origin.

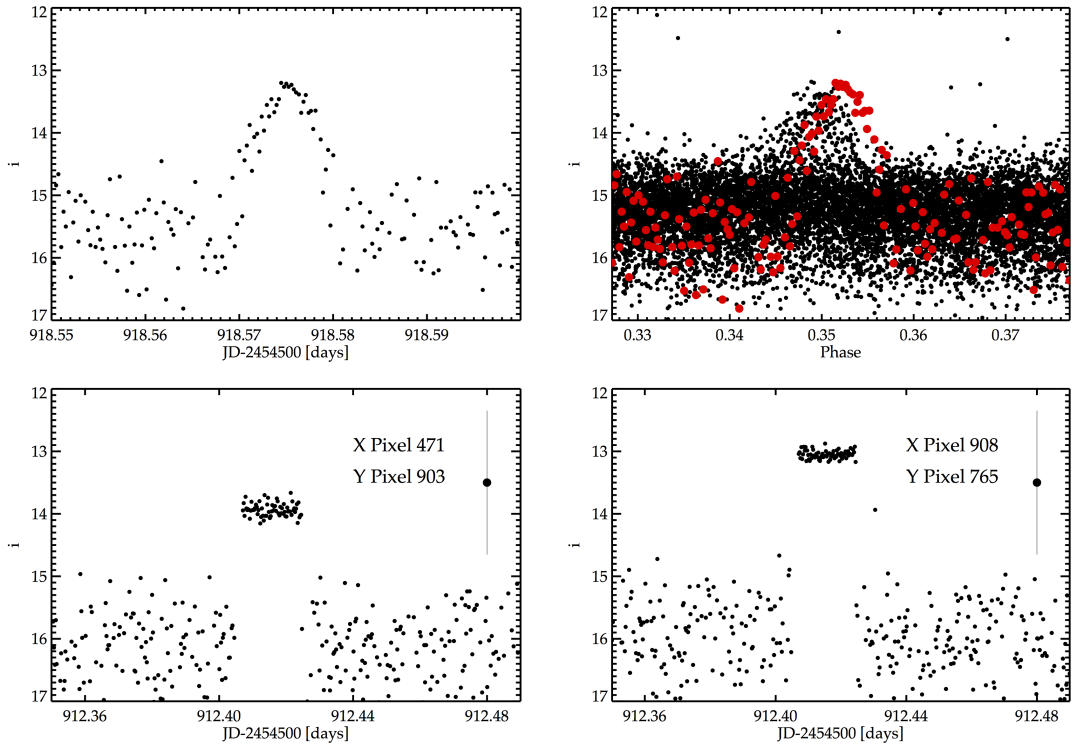

Figure 3.9: Impostor Transients
Top Left: The light curve of a transient candidate in i identified in a detection frame with a $\sim$ 2 mag variation that lasted for 0.01 d. *Top Right*: The same transient from the left phased on the sidereal day. The red data points mark the data points from the top left panel. A similar variation is seen near the same sidereal phase and therefore excludes the transient as a real candidate. *Bottom Panels*: Two separate transient candidates showing a sudden increase in flux that remains constant for the duration of the event. Both candidates are ruled out because of the simultaneous occurrence of the events. The typical error and (x,y) location is shown on the right of each panel.

3.6 Discussion

We have presented a technique useful for the reduction of crowded, defocused data. The 2009 Antarctic winter season observations by CSTAR at Dome A suffered from intermittent filter frosting, premature power failures and a defocused PSF. Even

with these technical issues the system obtained a total of $\sim 10^6$ scientifically-useful images in the 3 operating bands.

Each frame underwent extensive pre-processing including bias subtraction, flat fielding, background subtraction, electronic fringe subtraction and frame alignment. We used a combination of difference imaging with a delta function kernel and aperture photometry to compensate for the highly crowded, blending and defocused frames. We applied the Trend Fitting Algorithm and an alternative de-aliasing trend removal technique to correct for systematics resulting from detector variations or improper kernel fits.

We applied 3 variability tests, one periodicity search and one transit search to all light curves. We recovered 45 variable stars with highly significant variation within our magnitude limit ($g \sim r \sim 13.5$ mag, $i \sim 15$ mag) and identified 37 previously undiscovered variables in CSTAR data sets. Given the robust capabilities of the code and its proven ability to identify variable and eclipse events we are confident in the codes abilities to identify eclipses in variable objects. We therefore have elected to use this routine to reduce the wide-field data of young stellar associations as described in §4.

4. A WIDE-FIELD SEARCH FOR TRANSITING 'HOT JUPITERS' AND PRE-MAIN SEQUENCE BINARIES

Convinced our reduction methods were robust enough to detect planetary transits and stellar eclipses we conducted a wide angle search for transiting HJs and PMBs. We chose to use a wide-field, small-aperture imager to maximize the number of stars we could observe at any given time and we selected 3 young stellar associations to maximize our observing cadence.

4.1 The Survey Instrument

The imaging equipment, nicknamed "AggieCam", consisted of an Apogee Alta F16M camera, with a 4096 × 4096 pixel Kodak KAF-16083 CCD that is thermo-electrically cooled down to ΔT = -45°C relative to ambient. Testing of the CCD showed a dark current of 0.2 e/pix/s at temperatures of -25°C. The optics include a Mamiya photographic 300mm lens with a Hoya UV and IR cut filter to restrict the wavelength range from 4000 to 7000 Å. Total transmission of the system is near 45%. The pixel scale for the detector is 6.2″/pix, leading to a total FoV of nearly 50 square degrees. The system was deployed to the Bosque Alegre Astrophysical Station in collaboration with the Astronomical Observatory of Córdoba. The telescope was operated remotely from Texas A&M University from June 2013 - September 2014.

4.2 Targeted Young Stellar Associations

We targeted three young stellar associations to maximize the science return from our study: IC 2391 ($\alpha = 8^{\rm h}40^{\rm m}, \delta = -53°$), the η Chamaeleontis cluster ($\alpha = 8^{\rm h}45^{\rm m}, \delta = -79°$), and the Upper Scorpius association ($\alpha = 16^{\rm h}, \delta = -24.5°$). Given the spread in right ascension between IC 2391 and Upper Scorpius and the

circumpolar nature of η Chamaeleontis, we were able to make an efficient use of the camera all year long.

The Upper Scorpius association is a subsection of the larger Scorpius-Centarus association and it is the nearest OB association to the Sun (Preibisch et al., 2002). At a distance of 145 pc and a mean age of 11 ± 2 Myr (Pecaut et al., 2012) it is an excellent candidate for our survey. This association was chosen specifically for its large OBA membership ($\sim$100 confirmed members) which implies thousands of unconfirmed low-mass members (Rizzuto et al., 2015).

IC 2391 is a large, loose, young open cluster in Vela. Measurements of the main-sequence turn off and the lithium depletion boundary suggest an age of 30-50 Myr, while *Hipparcos* and Tycho-2 data led Reipurth (2008) to determine the distance to this cluster to be 147 ± 5 pc. This association was chosen because of its older population where we may expect to see transiting HJs if migration timescales are constrained by disk dissipation.

Lastly, the η Chamaeleontis cluster is located at a distance of 97 pc with confirmed stellar ages between $2 - 18$ Myr (Mamajek et al., 1999). η Chamaeleontis provides a variety of stellar ages to probe planetary formation, has a high number of confirmed T-Tauri stars and was chosen to ensure we could observe all year from Bosque Alegre.

4.3 Transit Survey Expectations and Achieved Observations

Previous studies of main-sequence stars in open clusters have shown the occurrence rate of HJs to be roughly 1% (Burke et al., 2006; Hartman et al., 2008; Bayliss & Sackett, 2011). Observationally, this translates to the detection of ~ 1 planet for every 5000 stars observed per month for transiting objects as shown by Burke et al. (2006). Our survey was expected to extend far beyond the one-month span required and we assumed we would detect multiple HJs. Under this assumption, even a null

result would yield a useful lower limit on the formation and migration time scales. Additionally, our observations could aid in the planning of future exoplanet studies. While each association does not contain the 5000 stars required to find one transiting HJ in one month's time, the planned survey duration of 3 years and *a priori* knowledge of some cluster members would allow selective targeting to determine the presence of young transiting HJs. It was also expected we would find transiting HJs around stars that have not yet been confirmed as cluster members due to the dearth of effective wide field surveys of each association.

As a proof of concept, we injected transit signals for a variety of HJs with a range of periods ($0.5 < P < 10$ d) and radii ($0.8 < R_J < 2.0$) into simulated light curves with dispersions based on the typical *rms* limits of the detector and calculated the number of hours of observation required for a detection that passed the criteria outlined above. We used the published distance to each association and the 30 Myr isochrones from Pietrinferni et al. (2006) and calculated the stellar mass and radius for a range of apparent magnitudes. Figure 4.1 shows we expected in 18 months we would have already achieved the required sensitivity over most of the target stellar types and by the end of 3 years all stellar types could be investigated.

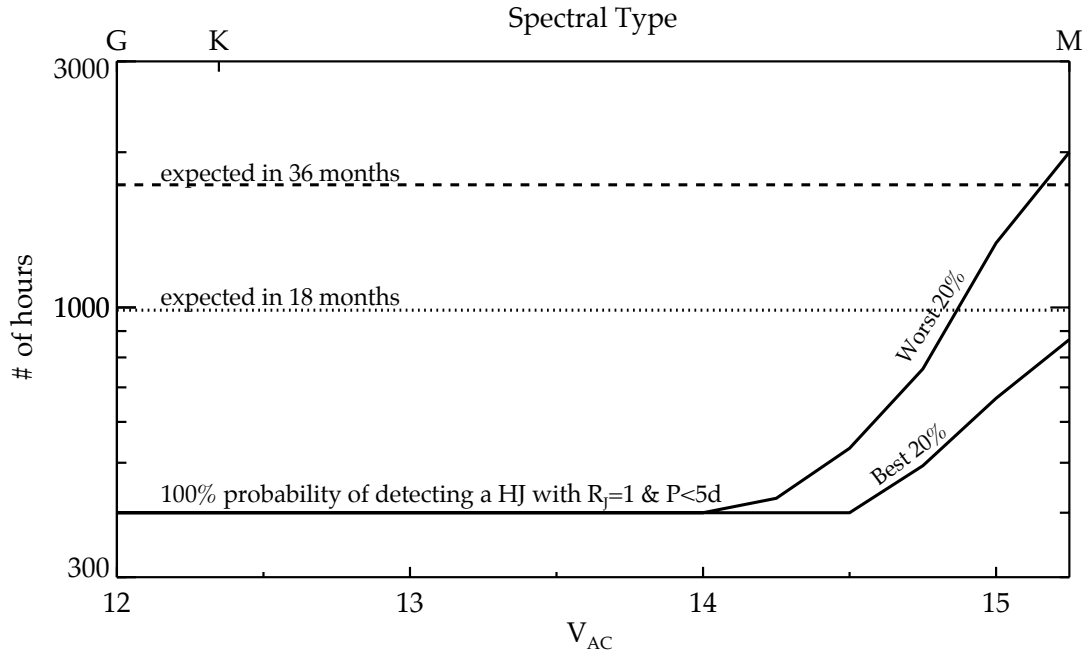

Figure 4.1: Hours of Observation Required to Detect a HJ
Hours of observation required to detect a 'Hot Jupiter' with P= 2.7 d and R= $1.5R_J$ as a function of magnitude and light curve dispersion. For $V_{AC} < 14$, 400 hr of observations are needed to capture three transits, while at fainter magnitudes the number of hours increases to account for the larger photometric dispersions. The dotted line denotes the number of hours per field after 1.5 years, while the dashed line represents the goal after 3 years of observation.

The final survey observations did not meet our expectations. The combination of an unprecedented rainy season at Bosque Alegre, technical support failures, a server failure and a lightning strike ended our survey after 15 months of observations with < 200 cumulative hours observed. Our monthly efficiency rate is shown in Figure 4.2. Figure 4.3 shows the final survey numbers for each association as 100 hours of observations for Upper Scorpius, 75 hours of observations for η Chamaeleontis and 40 hours of observations for IC 2391.

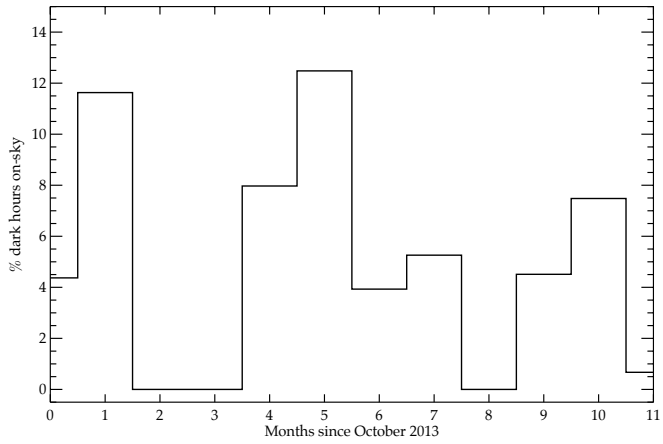

Figure 4.2: Observed Dark Hours
The percentage of dark hours that yielded useful data during each month of the 'AggieCam' observing campaign. The unprecedented weather conditions, coupled with technical failures, led to a very low total efficiency.

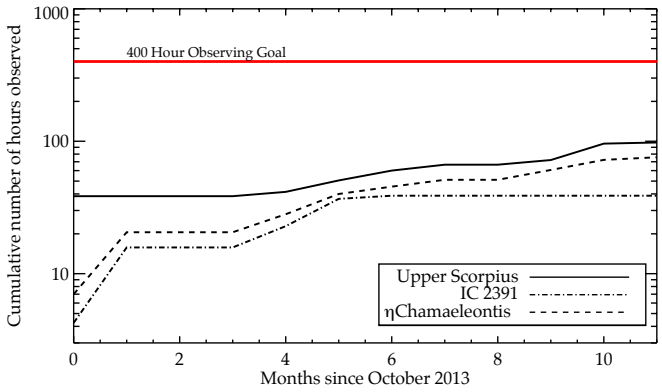

Figure 4.3: Total Observed Hours per Association
The cumulative number of observed hours per field after the month of October 2013. Upper Scorpius achieved 100 hours; η Chamaeleontis achieved 75 hours; and IC 2391 achieved 40 hours. No field reached the survey's goal of 400 hours of observation.

Fortunately, we were able to achieve our expected noise limits. Figure 4.4 shows our photometry reaching the expected scintillation and photon noise limits across each association. Bosque Alegre also proved to be a high-quality observing site when there were clear skies. Figure 4.5 shows that during observations with moon phase < 0.5 the mean sky brightness is 20.55 mag/arcsec^2 in V_{AC}.

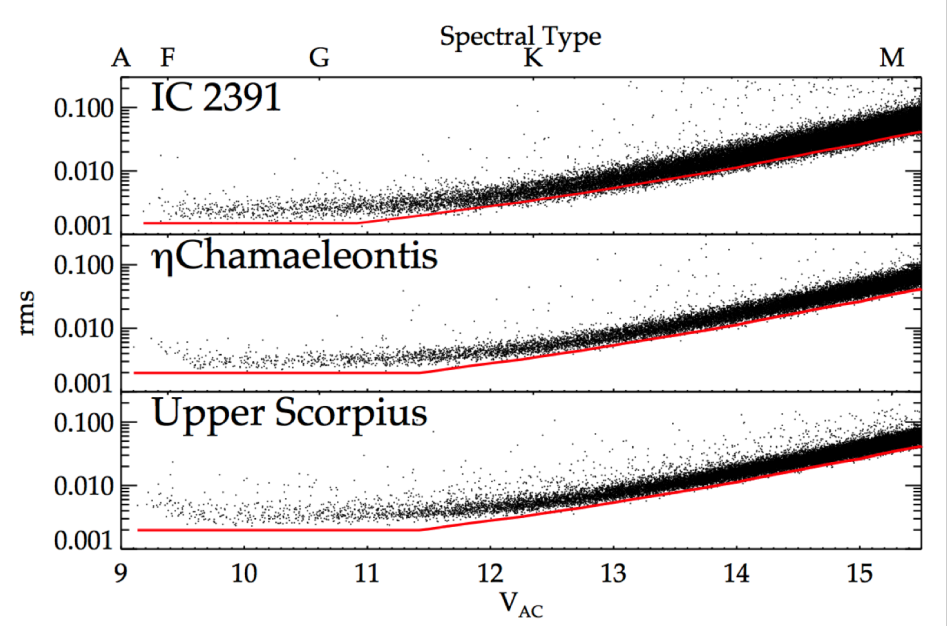

Figure 4.4: Achieved Photometric Precision of AggieCam
The achieved photometric precision of AggieCam in 30-minute intervals. The red line denotes the expected scintillation and star & sky noise limits.

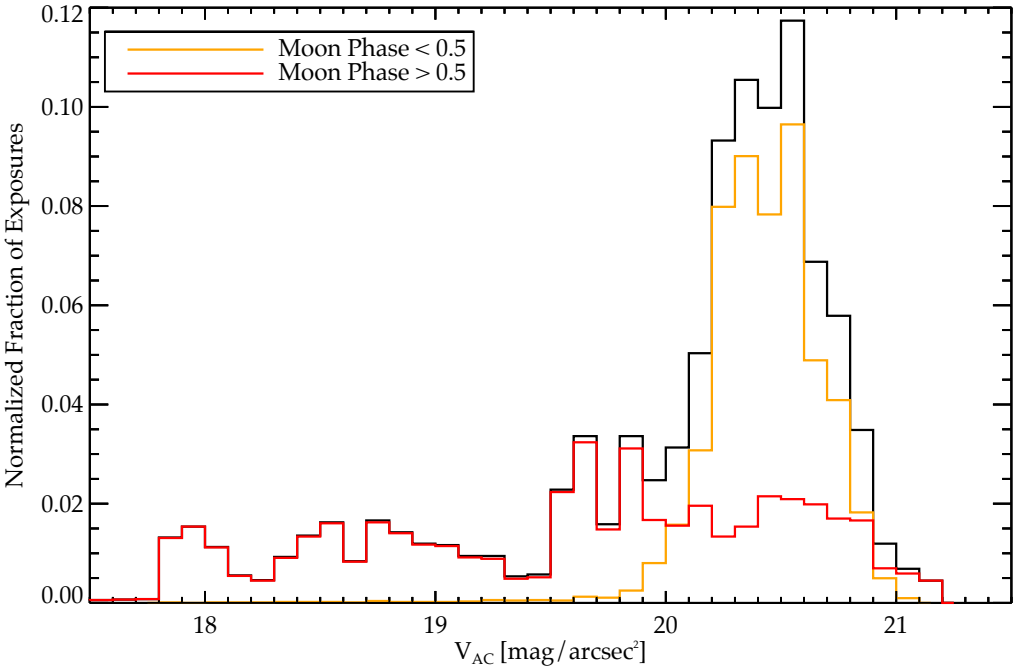

Figure 4.5: Sky Background from Bosque Alegre
The normalized number of exposures for varying sky brightness levels from Bosque Alegre. The median sky value under dark conditions (moon phase < 0.5) is 20.6 mag/arcsec^2.

4.4 Candidate Selection

As described in previous sections, we used a variety of variability and periodicity metrics to determine whether stars are variable or exhibited transits/eclipses. We briefly summarize them below.

4.4.1 Variable Objects

Following our previous searches for variable objects, we combined the 3 variability metrics (J_S, Δ_{90} & *rms*). We selected all objects greater than or equal to an iterative

3-sigma cut on the distribution of J values. For the Δ_{90} & *rms* statistics we selected all objects above the 2σ quartiles of each statistic. Any star passing each statistic was considered to be variable.

4.4.2 Periodic and Eclipsing Objects

We searched each light curve for periodic signals using LS as implemented in VARTOOLS (Hartman et al., 2008). We computed the 3 highest SNR periods of each star between 0.01 d and the total number of days observed for each association. Each light curve was whitened against the highest SNR period before searching for the next. We required each period to be unique and not lie on a known aliased period. We also applied $+3\sigma$ cuts on the false alarm probability ($\log_{10}$(FAP)) and cumulative SNR. The FAP provides an estimate on the likelihood of a true periodic signal by comparing the SNR of a specific signal to the cumulative distribution of all SNRs.

We searched for transit-like events using BLS (Kovács et al., 2002). Prior to the search we pre-whitened each light curve against the most significant LS period and its 10(9) (sub)harmonics. We also ran the search after pre-whitening the light curve with a B-spline to remove variation which could be aperiodic in nature. The duration of the transit was allowed to range in phase between 0.01 and 0.1 of the primary period with 10,000 trial periods and 200 phase bins. Each object passing the LS & BLS tests was visually inspected to confirm the periodic nature and to identify binary or planetary candidates.

4.4.2.1 Transit Candidate Requirements

The search was conducted between 0.1 and $\frac{1}{3}$ of the total days observed per association in order to ensure we observed *at least* 3 transit events. We required each period to be unique and have a unique ephemeris time to avoid contamination

by aliased periods. We also required the ratio of $\chi^2/\chi^2_- > 1.5$. The $\frac{\chi^2}{\chi^2_-}$ statistic shows how well a transit model is fit compared to a transit model fit to the inverted light curve (Burke et al., 2006). Light curves with $\chi^2/\chi^2_- << 1$ are ill-suited for transit searches. Finally we required the signal-to-pink noise statistic (hereafter, SPN) to be greater than 5. The SPN tracks how significant a specific transit period is compared the noise model of the light curve. Candidates passing these 3 metrics were considered genuine.

4.4.3 Results of the Search

Employing the metrics above, we discovered over 5,000 variable candidates across all 3 fields with $\sim 20\%$ of the objects showing a statistically-significant period. Figure 4.6 shows 15 expected variable candidates from all 3 fields. 368 of these objects showed a possible binary eclipse. The majority of these pre-main-sequence binary (PMB) candidates had periods P$<$ 10 d. This is not surprising given the short duration of the observations in each field.

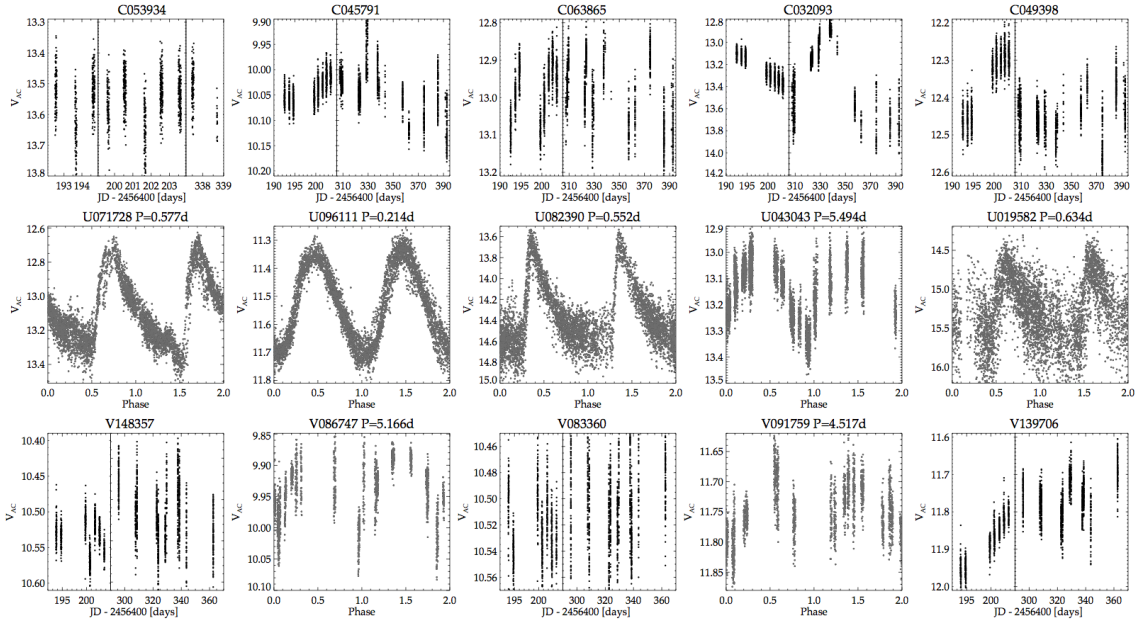

Figure 4.6: AggieCam Variable Candidates
15 variables found in each association as part of our search. The typical error is shown at the bottom right of each panel. If a significant period was identified as part of the search it is displayed in the title of the panel.

The results of the search for Hot Jupiters provided 7 potential candidates. 6 candidates were from the Upper Scorpius field and 1 was from η Chamaeleontis. Unsurprisingly no candidates were identified in the IC 2391 data. This is likely due to the small relative number of observations taken in the field. All Hot Jupiter candidates had periods P$<$ 6 d with 3 objects having P$<$ 1 d. Figure 4.7 shows a collection of the HJ and PMB candidates.

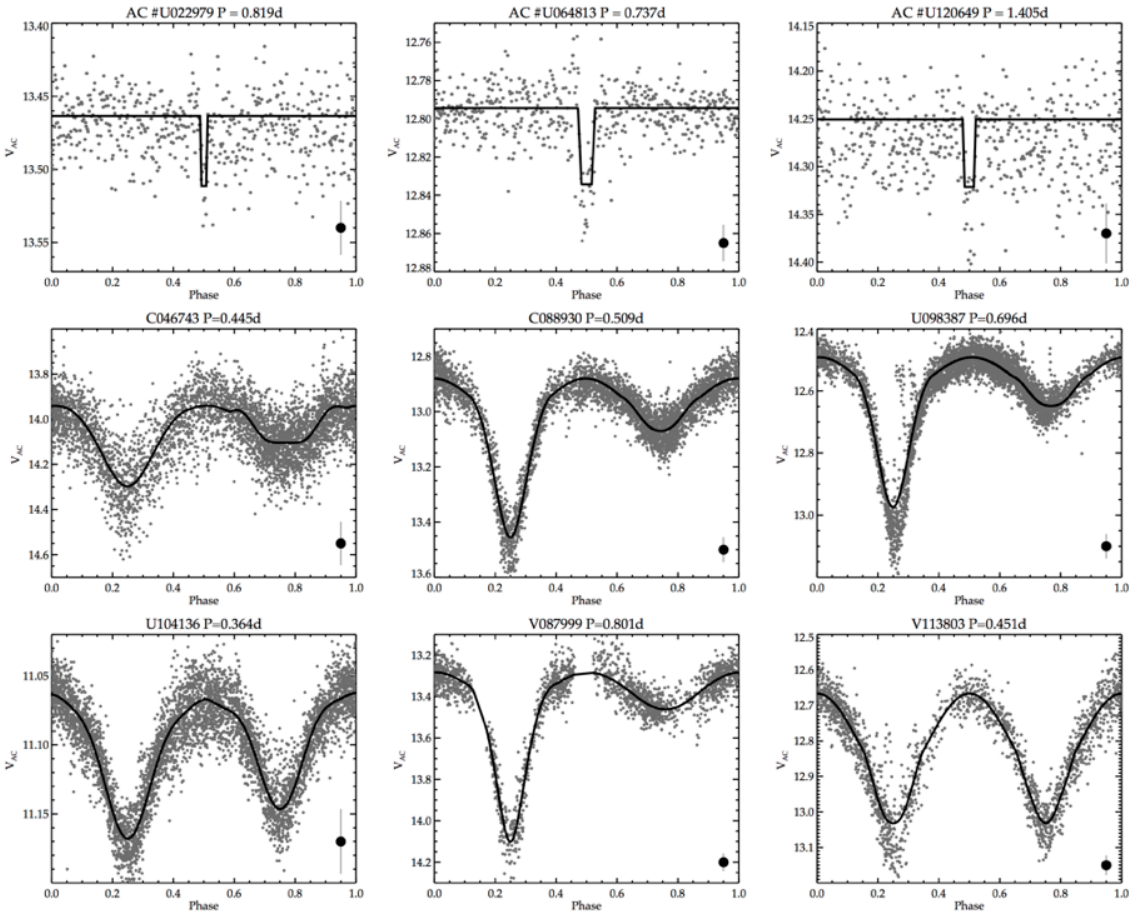

Figure 4.7: AggieCam HJ and PMB Candidates
[Top Row] Three HJ candidates of various periods, detected at high significance as part of our search. The black line denotes the best-fit BLS model of the transit.[Middle & Bottom Row] 6 PMB candidates from each association. The black lines denote the best fit JKTEBOP model. Errors are shown in the bottom right of each figure.

4.5 Higher Precision Photometric Follow-Up

Any transiting HJ or PMB candidate passing all of the above significance tests was then subjected to a series of follow-up photometric observations. These observa-

tions are used to provide independent, higher-precision transit and eclipse measurements. They also helped to confirm and refine the orbital period, depth, ephemeris and duration for each eclipse. In the case of transiting HJ candidates, the time of secondary eclipse was probed to ensure no large variations in flux occurred, which would indicate a grazing EB or background blend. The higher angular resolution of the telescopes also allowed us to determine any contamination from blending due to the coarser pixel scale ($6''$/pix) of AggieCam. These observations also provided color measurements which helped to identify spectral type, binary contamination in the HJ sample and association membership.

The 1.54 m telescope at Bosque Alegre provided 300+ hrs of BRVI photometry and is currently ongoing; the McDonald Observation 0.8 m telescope provided 14 hrs in BVRI; the 1 m Las Cumbres Global Observatory Telescope (LCOGT) Network provided 30 hrs in *gri*; and the 0.5 m telescope at Texas A&M University provided 30 hrs in *gri*.

We ruled out all 7 transiting candidates using these higher precision measurements. We believe we identified these systems as HJ because of low-level variable activity. Our higher-precision measurements showed significant pulsations likely due to magnetic activity, stellar rotation and the star-spot cycle. We hypothesize this created periodic changes in the light curve which was flagged as genuine in our programs and because of the small number of observations we were unable to identify this variability prior to follow up. Follow up observations have been completed for 40 PMBs and are ongoing for another 328 systems.

4.6 Results

4.6.1 The Migration Timescale for Hot Jupiters

We were unable to identify any genuine transiting HJs as part of our sample. Before we can speculate on the scientific implications of our null result we need to properly assess our ability to detect these objects and identify any potential biases. We can do this by answering two questions to determine the confidence on our null result: 1) How many HJs should exist in these associations? 2) If a HJ exists, would we have detected it?

4.6.1.1 How Many Hot Jupiters Should Exist in This Field?

Previous studies of main-sequence stars have determined the planet fraction of Hot Jupiters is $P_{frac} =\sim 1\%$. This means that for every 100 stars, 1 should host a Hot Jupiter. However, if we look at the expectations for the planet fraction of Very Hot Jupiters (P$<$ 3 d) we find the expected planet fraction is even smaller at $P_{frac} =\sim 0.1\%$ (Fressin et al., 2013). This means that for every 1000 stars, 1 should host a Very Hot Jupiter. Because our association membership is typically between 100-1000 members, extra care needs to be given to interpreting our null result. By combining these planet fractions with the detection probabilities below, we can determine if our null result is consistent with the expectation of HJ migration due to disk accretion (Type I and II migration).

4.6.1.2 If a Hot Jupiter Exists, Would We Have Detected It?

We determine our detection probability following the same logic as Burke et al. (2006) with the full detection probability being defined as

$$P_{det,i} = \int\int \frac{d^2p}{dR_p da} P_{\epsilon,i}(a, R_p) P_{T,i}(a, R_p) P_{mem,i} dR_p da \tag{4.1}$$

where R_p is defined as the planet radius; a is the semi-major axis; $P_{\epsilon,i}(a, R_p)$ is the probability of detecting a transit around the i^{th} star in the survey averaged over orbital phase and inclination; $P_{T,i}(a, R_p)$ is the probability a planet of R_p and a would transit its host star; $P_{mem,i}$ is the probability the i^{th} star is a member of the association.

We calculate $P_{\epsilon,i}$ by injecting transiting objects into fake light curves of similar dispersion and observation cadence with varying orbital periods and transit durations. We then run the same detection statistic described above and determine the recovered fraction of transiting systems. The calculation of $P_{T,i}$ is independent of our survey data. If we assume a random inclination orientation of a star with respect to the observer then $P_{T,i} = \frac{R_* + R_p}{a}$ where R_* is the radius of the star. This calculation was integrated into the above calculation of P_ϵ with uniform distributions of inclination angles. In simpler terms $P_{T,i} = \int_0^i cos(z)dz$ where i is defined as all observable inclination angles. Finally the calculation of $P_{mem,i}$ is based on the proper motion and infrared colors of each star. The specifics for these tests are described in § 4.6.2.

4.6.1.3 Implications of the Null Result

To interpret our results we can consider two hypotheses for the migration timescales of HJs.

- H_0: HJs migrate in less than 10 Myr
- H_a: HJs migrate in more than 10 Myr

We assume that every HJ is formed and migrates on roughly the same timescale. Therefore, by observing each young stellar associations of different ages every HJ in the association has either migrated or none of the HJs in the association have migrated. For a particular star, the probability of finding a HJ is a combination of

$P_{det}P_{frac}$, where P_{det} is the detection probability calculated above and P_{frac} is the expected planet fraction based on previous studies of evolved stars.

We will let X = the total number of HJs found. Based on the above considerations, if the null hypothesis is true (H_0 is true) X is a binomial random variable which means

$$P_{H_0}(X = 0) = \binom{n}{x}(P_{det}P_{frac})^x(1 - P_{det}P_{frac})^{n-x} \tag{4.2}$$

for $x = 0, ..., n$, where n is the total number of stars observed. Therefore our expectation for the number of HJs which could be found is

$$E[X] = \sum_{x=0}^{n} x\binom{n}{x}(P_{det}P_{frac})^0(1 - P_{det}P_{frac})^n = (1 - P_{det}P_{frac})^n \tag{4.3}$$

If the alternative hypothesis is true, then $P_{H_a}(X = 0) = 1$ because there would not be any HJs detected. Therefore the p-values for this hypothesis test is given by computing

$$P_{H_0}(X = 0) = \binom{n}{0}(P_{det}P_{frac})^0(1 - P_{det}P_{frac})^n = (1 - P_{det}P_{frac})^n \tag{4.4}$$

A lower p-value would suggest more evidence for the alternative hypothesis. We see our expectation value for a HJ in Upper Scorpius is $E[X]$=34% for P$< 0.5d$ and quickly drops off as the period is increased or we move to fainter magnitudes (see Figure 4.8). We can interperet this value as 1 minus the p-value using the equations above. Therefore, we cannot outright reject the null hypothesis. We see our null result is consistent with the expected fraction of HJs with such short periods as shown in Figure 4.9. While the confidence on these results are not significantly constrained, we can still make an interesting interpretation.

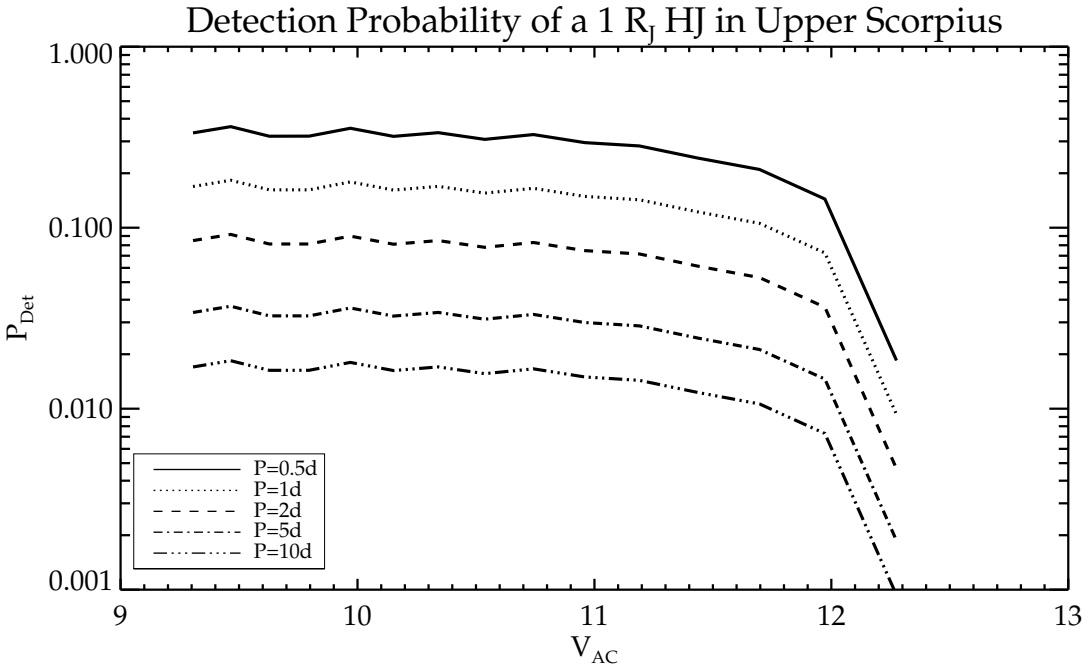

Figure 4.8: HJ Detection Probability

The probability of detecting a HJ in our sample as a function of magnitude for stars in Upper Scorpius. The probability of detecting a HJ with P$<$ 0.5 d is $\sim$ 37% for $V_{AC} < 12$ and quickly declines for longer periods and fainter magnitudes.

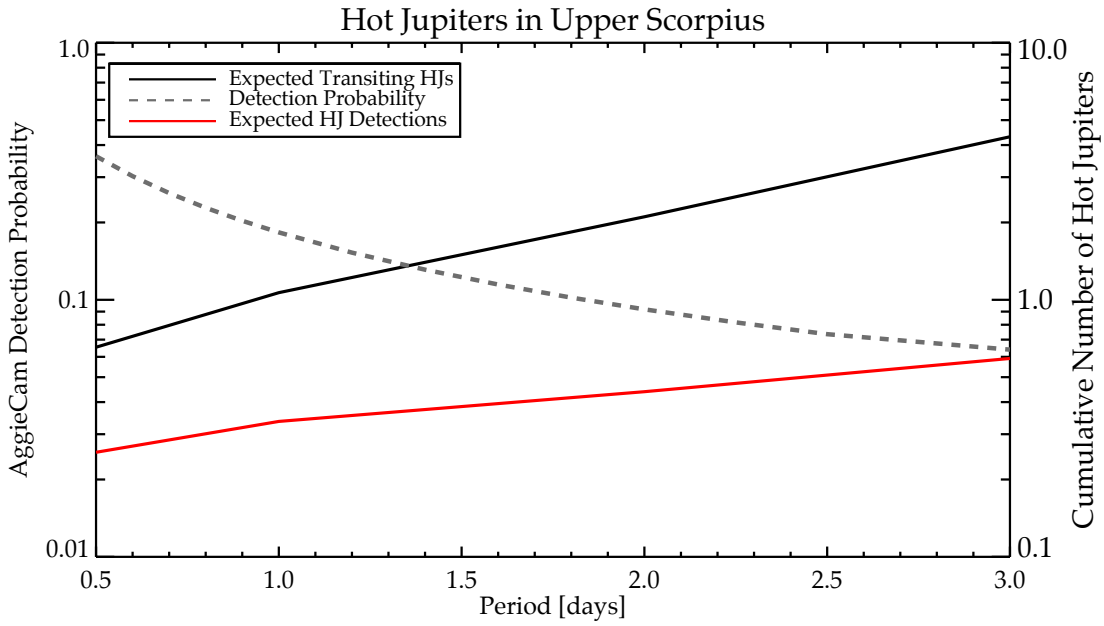

Figure 4.9: Expected Number of HJs in Upper Scorpius
The cumulative number of expected HJs in the Upper Scorpius association as a function of period. The black line denotes the number of HJs detected with 100% efficiency while the red line denotes our expected detection rate. The grey line is our detection efficiency as a function of orbital period. At $P = 0.5$ d where, we are most likely to detect planets, we find our null result is consistent with expectation that < 1 HJ would exist with such a period.

If we have not detected any HJs because they do not exist, and not simply as an artifact of the low number of observations, we can then attempt to understand the implications for the migration timescale. Because disk formation, accretion and dissipation is expected to be finished by 10 Myr, it is surprising the planets have not yet migrated to their 'Hot' positions. Both Type I and II migration require an actively accreting disk to move the planet inwards towards its host star (Ida & Lin, 2008). Similarly, recent studies have also suggested *in-situ* HJ formation and that

the snow line may not be a requirement for primary atmosphere retention (Batygin et al., 2015). Our result does not help to confirm either hypothesis.

The lack of observed transiting HJs appears to support the planet scattering processes or planet capture. Our null result and planet scattering is also supported by the relatively large orbital inclination angles of the majority of the known confirmed HJs. In this scenario, it is much more likely large Jupiter sized planets form with a similar mass outer companion. These two objects experience a Kozai scattering and the small body is ejected while the larger body migrates towards the host star. This theory can also be strengthened by current observations which show "warm" Jupiters with similar distant gas companions (Huang et al., 2016).

4.6.2 Binary Candidate Membership Confidence

The AggieCam survey identified more than 300 PMB candidates. All of these objects require higher-precision photometric and spectroscopic follow up to properly classify the objects as genuine PMS objects and have their stellar parameters measured. However, the spectroscopic follow up of more than 300 objects is not a trivial task. The stars must be prioritized in order to efficiently use assigned telescope time. We ranked each of the PMB candidates on a scale of 0 (low-priority) to 7 (high-priority) as described below. This was done using archival 2MASS & WISE colors to determine infrared excess (Skrutskie et al., 2006; Wright et al., 2010), using the UCAC4 proper motion catalogue to compare the motion of a given candidate with the mean of its putative association (Zacharias et al., 2013), inferring possible component masses based on eclipse depth & apparent magnitude and high-resolution spectroscopy to search for the Li I line at 6708Å for 7 initial test binaries.

4.6.2.1 Color Selections

An infrared excess is used to describe an object which appears to have a normal spectral energy distribution in the ultraviolet and visible wavelengths but shows a large excess of flux at infrared wavelengths. These excesses manifest themselves in young stellar objects because these stars are typically enshrouded in a dusty proto-stellar disk which absorbs ultraviolet light and re-emits it in the infrared.

To determine which stars may show these infrared excess, we investigate the 2MASS and WISE archival photometry (Skrutskie et al., 2006; Wright et al., 2010). We combined the *J-H* v.s *H-K* color-color diagram with the stellar locus provided by Pecaut & Mamajek (2013) to estimate the spectral type of each binary star. If the star was within 2σ of a particular point in the locus we deemed the photometry to be accurate enough to estimate the spectral type.

Following the methodology of Luhman & Mamajek (2012); Rizzuto et al. (2015) we made color cuts using 2MASS K-band photometry and the WISE W2, W3 and W4 bands. Stars lying above the lines denoted in Figure 4.10 are expected to show infrared excess indicative of a younger stellar population. These boundaries are the expected photospheric flux visible *after* dissipation of the proto-planetary disk. Binaries showing these excesses were flagged as high-priority candidates, with each excess adding an additional point to the total priority score.

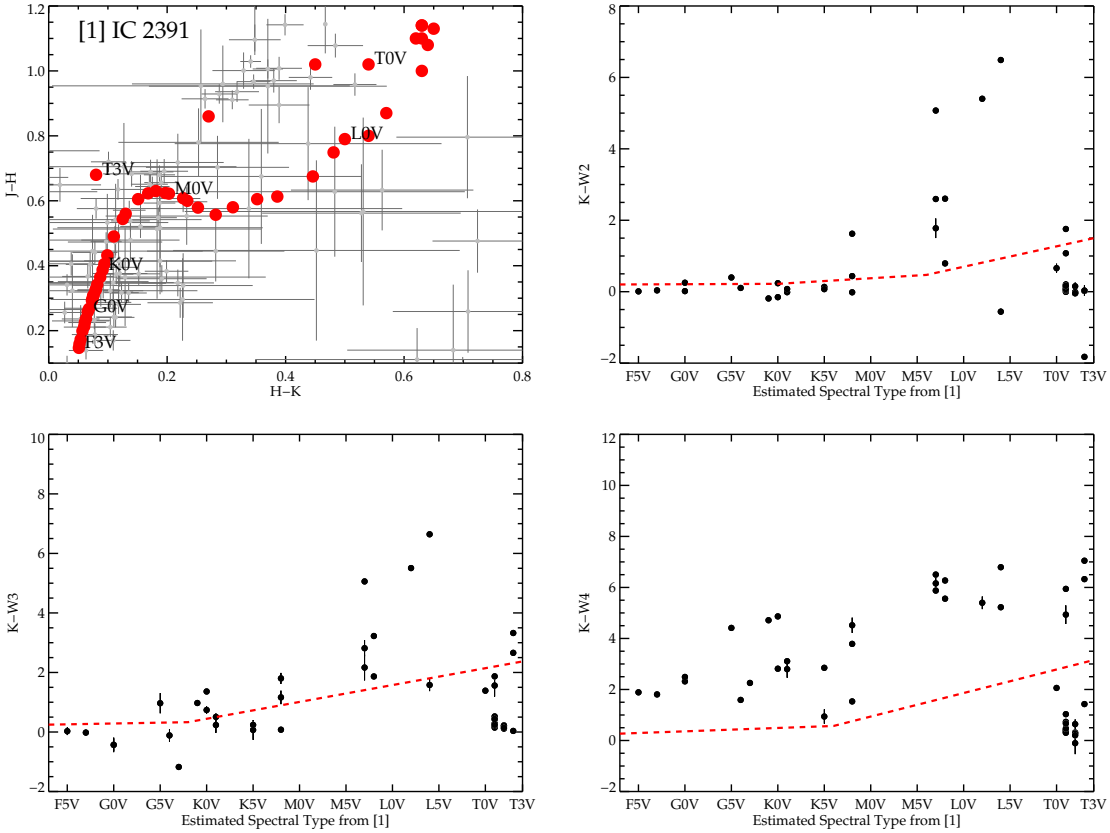

Figure 4.10: 2MASS & WISE Color Excess

[Top Left] 2MASS color-color diagram and stellar locus from Pecaut & Mamajek (2013). Stars were assigned with a specific spectral type if they were located within 2σ of a particular main-sequence data point in the locus. [Top Right, Bottom Left & Bottom Right] (K-W2 (W3,W4)) vs estimated spectral type diagram. Stars lying above the red lines are considered to have an excess amount of flux in the infrared, indicative of an accretion disk. The red dotted line marks where the expected photospheric excess ends for main-sequence objects (Luhman & Mamajek, 2012; Rizzuto et al., 2015).

4.6.2.2 Proper Motions

We used the proper motions from the UCAC4 catalogue (Zacharias et al., 2013) to identify objects which show similar motions to the well studied O/B/A/F stars

in each association. Using the measured mean proper motions of each association from previous studies (Dodd, 2004; Luhman & Mamajek, 2012; Lopez Martí et al., 2013) and the expected 15-20 mas error of the UCAC4 catalogue, we identified all candidate binaries which were within 3σ of the mean proper motion. Only stars with measured proper motions were included in our significance testing. We subtracted 1 point from the priority score for each σ a candidate's proper motion was separated from the mean proper motion of the association: $1\sigma = 3$ points, $2\sigma = 2$ points, $3\sigma = 1$ points, $> 3\sigma$ or no measured motion$= 0$ points. Figure 4.11 shows measured proper motions for the binary candidates and their positions in the AggieCam FoV.

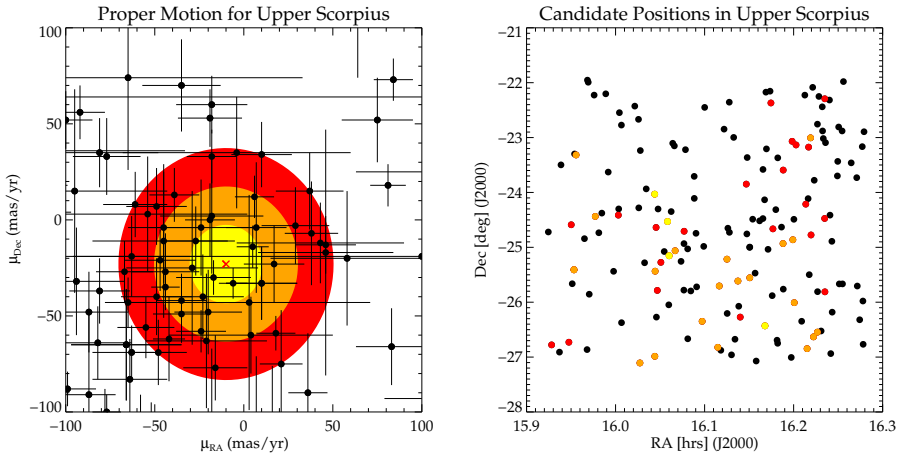

Figure 4.11: Proper Motion Selections
[Left] The measured proper motions of stars in the Upper Scorpius field with measured proper motions from the UCAC4 catalogue plotted with their 1σ error bars. Objects were selected as likely candidates based on their position relative to the mean proper motion of the moving group. The colored regions denote 1, 2 & 3 σ errors of the UCAC4 catalogue: yellow, orange and red respectively. [Right] The position of each PMB candidate in the FoV of AggieCam. The coloring of the points relates to the proximity of the proper motion of a given star to the mean of the association: red (3σ), orange (2σ) and yellow (1σ). A black dot means the star either was too far from the mean motion or did not have a well-measured proper motion in UCAC4.

4.6.2.3 Testing Viable Binary Components

The component masses of the system can still be estimated even without proper spectroscopic observations. The ratio of the eclipse depths is proportional to the ratio of the temperatures of the photospheres of the stars. This ratio can then be used in conjunction with the apparent magnitude and expected distance of the association to place limits on the masses of the components *if* they are assumed to be at the distance of the association.

We fit a parabola to both the primary and secondary eclipse using the IDL routine POLY_FIT to determine the minimum flux value. We then calculated the ratio of the effective temperatures as follows:

$$(\frac{T_S}{T_P})^4 = \frac{F_0 - F_P}{F_0 - F_S} \tag{4.5}$$

where F_0 is the flux at quadrature and F_P & T_P are the flux during the primary eclipse and effective temperature of the primary star respectively (an S denotes the secondary).

The distance modulus was calculated using the distance to each association and subtracted from the apparent magnitude of the system to determine the expected absolute magnitude of the system. The Spada et al. (2013) zero-age-main-sequence isochrones were employed to calculate the magnitudes of the components which could be combined to generate this magnitude based on the temperature ratio. Kepler's third law was used to calculate the separation of the system using the known period. We determined the viability of each binary based on the orbital separation and the shape of the light curve. For example, a binary composed of two K-dwarfs with a separation of 1 solar radii should be in a nearly contact system and *not* a detached system. If the system was deemed viable it was given 1 point toward its priority

score.

4.6.2.4 Spectroscopy

Preliminary spectroscopy was obtained for 7 PMB candidates at McDonald Observatory during the Spring of 2015. The combination of spread in ephemeris timing and poor observing conditions only allowed each PMB to be observed once during quadrature. Nevertheless, these measurements provide valuable information about the radial velocity and spectral types for each system. We obtained the spectra using the Sandiford Echelle Spectrograph (hereafter, SES) on the 2.1 m at McDonald Observatory. Thorium-Argon exposures bracketed the science observations and were used to wavelength-calibrate the data using the IRAF routine REFSPEC. The radial velocities were calculated using a cross-correlation with reference spectra taken on the same night and spectral templates from SDSS DR5. While the SNR of our spectra were particularly low (< 10) we were still capable of achieving $1 - 5$km/s precision on each radial velocity measurement through the cross-correlation.

We then subjected the detection light curve, followup multi-color photometry and initial estimates of the radial velocity to the JKTEBOP binary fitting program (Southworth et al., 2013). JKTEBOP models each component of a binary as a sphere for calculating the eclipse shapes and a biaxial ellipsoid for calculating proximity effects. The program uses Levenberg-Marquardt optimization to find the best fit model. An example of a binary being subjected to this fitting process is shown in Figure 4.12

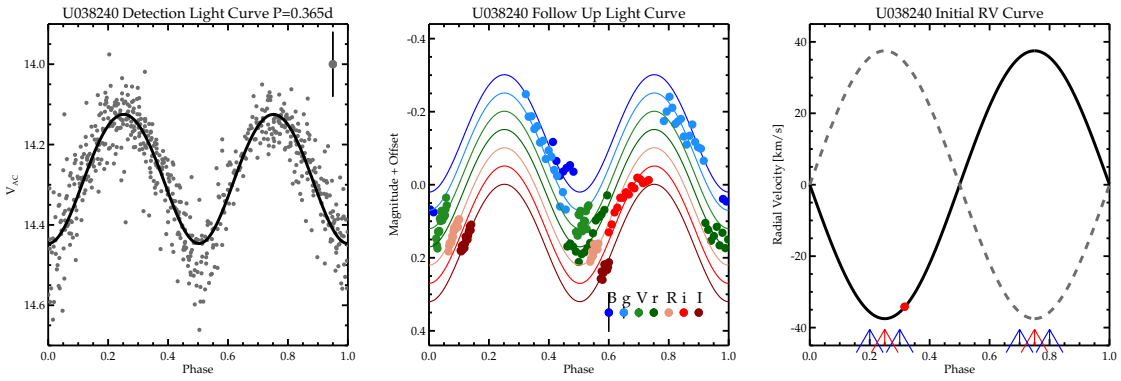

Figure 4.12: Radial Velocity of a PMB Candidate
PMB candidate U038240 discovered in Upper Scorpius at each stage of the classification process: detection [top]; multi-color follow up [middle]; initial RV measurements [bottom]. The solid lines denotes the best-fit JKTEBOP models (Southworth et al., 2013). The expected RV variation is extrapolated from the eccentricity of the system and the best-fit orbital parameters of JKTEBOP. The blue arrows denote the acceptable range of observation in phase and the red arrows denote exact quadrature.

4.6.2.5 Discussion and Future Study

Although our observations were plagued with bad weather, technical set-backs and a lightening strike, we were able to reach the necessary precision for an exoplanet & eclipsing binary search even with our minimal observations. We detected more than 300 pre-main-sequence binary candidates and identified 7 Hot Jupiter candidates which were ruled out with higher-precision followup observations.

In order to properly interpret our null result we determined our detection probability to be 34% for HJs with $P < 0.5$ d. This detection probability, coupled with a low expected number of HJs at those periods, suggest our null result is consistent with expectations. Nevertheless, our determined Hot Jupiter migration timescale is > 11 Myr. If this migration timescale is to be believed then it has implications

on the timescales for planet formation. This timescale rejects the theory of *in-situ* formation out-right and suggests planets can migrate towards their host star on time scales longer than disk formation, accretion and dissipation. This would suggest planet scattering or mean motion resonances play a much larger role on solar system formation. This hypothesis is supported by the large number of HJs which show large orbital inclination angles relative to their host stars rotation angle.

Finally, we identified 368 candidate pre-main-sequence binary stars. 12% of these stars show an infrared excess, 30% of these stars show similar proper motions to the known proper motion of the association and 89% have temperature ratios which are consistent with two zero-age-main-sequence stars. We have prioritized these stars for future follow up.

5. CONCLUSIONS

We have presented the results of a wide-field survey for transiting HJs and PMBs in young stellar associations. The survey collected over 200 hours of observation of 3 separate young stellar associations: Upper Scorpius, η Chamaeleontis and IC 2391. We reduced this data using proven photometric reduction techniques including a robust search for eclipse events.

These photometric reduction techniques rely on precise image calibration through bias subtraction, flat fielding, sky subtraction, electronic pattern subtraction, image alignment, difference image analysis, aperture photometry and the use of the Trend Filtering Algorithm. These techniques are novel because they implement a Dirac-δ function kernel to accurately model any shape PSF. Using these methods our data products were only bound by photon noise and atmospheric scintillation.

We tested these techniques on the CSTAR photometric data set from Dome A in Antarctica prior to our search of young stellar associations. This data set is large ($> 10^6$ images), multicolor (*gri* & *clear*) and required advanced calibration. We searched for regular variable stars using the combination of the Stetson-Welch J statistic, rms and Δ_{90}. We searched for periodic variables using the Lomb-Scargle algorithm and the Box-Least-Squares algorithm. We identified more than 200 likely variable stars, 44 of which showed highly significant variation, across 15,380 light curves. These stars included irregular variables, RR Lyraes, δ Scutis, γ Doradus, contact binaries, semi-detached binaries, detached binaries, planet transit candidates and multi-periodic variable stars. We were also able to successfully recover eclipse events in variable stars which appear to show significant variability including a Type II Cepheid in an eclipsing system.

Additionally the improved photometry delivered by this technique enabled us to search for stellar flares and to better characterize classical (and in some cases periodic) variables. We identified 29 flaring events implying a flare rate of $3\pm1\times10^{-7}$ flare/hr for the entire CSTAR field, $2\pm1\times10^{-7}$ for Late K and $6\pm3\times10^{-7}$ flare/hour for M dwarfs and in the halo. The generation of "detection frames" for the transient search enabled us to identify a large number of systematic effects, some of which have resulted in the erroneous claim of astrophysical variability in previous analyses of these data sets.

Satisfied our analysis was capable of reaching the required precision, we searched our young stellar association data set. Although our observations were plagued with bad weather, technical set-backs and a lightening strike we were able to reach the required precision even with our minimal observations. We detected more than 300 pre-main-sequence binary candidates and identified 7 Hot Jupiter candidates which were ruled out with higher precision follow up.

In order to properly interpret our null result we determined our detection probability to be 34% for HJs with $P < 0.5$ d. This coupled with the low expected number of HJs at those periods suggest our null result is consistent with expectations. Nevertheless our determined HJ migration time scale is > 11 Myr. This migration timescale has implications on the models of planet formation. This timescale rejects the theory of *in-situ* formation out-right and suggests planets can migration towards their host star on time scales longer than disk formation, accretion and dissipation. This would suggest planet scattering or mean motion resonances play a much larger role on solar system formation. This hypothesis is supported by the large number of HJs which show large inclination angles relative to their host star's rotation angle.

Finally we identified 368 candidate pre-main-sequence binary stars. 12% of these stars show an infrared excess, 30% of these stars show similar proper motions the

known proper motion of the association and 89% have temperature ratios which are consistent with two zero-age-main-sequence stars. We have prioritized these stars for future followup.

REFERENCES

Alard, C. 2000, Astronomy and Astrophysics, Supplement, 144, 363

Alard, C., & Lupton, R. H. 1998, The Astrophysical Journal, 503, 325

Baglin, A., Michel, E., Auvergne, M., & COROT Team. 2006, in ESA Special Publication, Vol. 624, Proceedings of SOHO 18/GONG 2006/HELAS I, Beyond the spherical Sun, 34.1

Bakos, G. Á., Lázár, J., Papp, I., Sári, P., & Green, E. M. 2002, Publications of the Astronomical Society of the Pacific, 114, 974

Baraffe, I., Homeier, D., Allard, F., & Chabrier, G. 2015, Astronomy and Astrophysics, 577, A42

Batygin, K., Bodenheimer, P. H., & Laughlin, G. P. 2015, ArXiv e-prints, arXiv:1511.09157

Bayliss, D. D. R., & Sackett, P. D. 2011, The Astrophysical Journal, 743, 103

Borucki, W. J., Koch, D., Basri, G., Batalha, N., Brown, T., et al. 2010, Science, 327, 977

Burke, C. J., Gaudi, B. S., DePoy, D. L., & Pogge, R. W. 2006, The Astronomical Journal, 132, 210

Charbonneau, D., Brown, T. M., Latham, D. W., & Mayor, M. 2000, The Astrophysical Journall, 529, L45

Davenport, J. R. A., Becker, A. C., Kowalski, A. F., Hawley, S. L., Schmidt, S. J., et al. 2012, The Astrophysical Journal, 748, 58

Davenport, J. R. A., Hawley, S. L., Hebb, L., Wisniewski, J. P., Kowalski, A. F., et al. 2014, The Astrophysical Journal, 797, 122

Dodd, R. J. 2004, Monthly Notices of the Royal Astronomical Society, 355, 959

Duchon, J. 1976, ESAIM: Mathematical Modelling and Numerical Analysis - Modélisation Mathématique et Analyse Numérique, 10, 5

Exoplanet Orbit Database. February 19, 2016, Exoplanets Data Explorer, exoplanets.org

Fitzpatrick, E. L. 1999, Publications of the Astronomical Society of the Pacific, 111, 63

Fressin, F., Torres, G., Charbonneau, D., Bryson, S. T., Christiansen, J., et al. 2013, The Astrophysical Journal, 766, 81

García, R. A., Ceillier, T., Salabert, D., Mathur, S., van Saders, J. L., et al. 2014, Astronomy and Astrophysics, 572, A34

Girardi, L., Barbieri, M., Groenewegen, M. A. T., Marigo, P., Bressan, A., et al. 2012, TRILEGAL, a TRIdimensional modeL of thE GALaxy: Status and Future, ed. A. Miglio, J. Montalbán, & A. Noels (London: Springer-Verlag Berlin Heidelberg), 165

Grossmann, V., Baessgen, G., Evans, D. W., Grenon, M., Grewing, M., et al. 1995, Astronomy and Astrophysics, 304, 110

Hartman, J. D., Gaudi, B. S., Holman, M. J., McLeod, B. A., Stanek, K. Z., et al. 2008, The Astrophysical Journal, 675, 1254

Hartman, J. D., Stanek, K. Z., Gaudi, B. S., Holman, M. J., & McLeod, B. A. 2005, The Astronomical Journal, 130, 2241

Hawley, S. L., Davenport, J. R. A., Kowalski, A. F., Wisniewski, J. P., Hebb, L., et al. 2014, The Astrophysical Journal, 797, 121

Henry, G. W., Marcy, G. W., Butler, R. P., & Vogt, S. S. 2000, The Astrophysical Journall, 529, L41

Howell, S. B., Sobeck, C., Haas, M., Still, M., Barclay, T., et al. 2014, Publications of the Astronomical Society of the Pacific, 126, 398

Huang, C. X., Wu, Y., & Triaud, A. H. M. J. 2016, ArXiv e-prints, arXiv:1601.05095

Ida, S., & Lin, D. N. C. 2008, The Astrophysical Journal, 673, 487

Jofré, P., & Weiss, A. 2011, Astronomy and Astrophysics, 533, A59

Kaluzny, J., Stanek, K. Z., Krockenberger, M., Sasselov, D. D., Tonry, J. L., et al. 1998, The Astronomical Journal, 115, 1016

Kennicutt, R. C., & Evans, N. J. 2012, Annual Review of Astronomy and Astrophysics, 50, 531

Kovács, G., Bakos, G., & Noyes, R. W. 2005, Monthly Notices of the Royal Astronomical Society, 356, 557

Kovács, G., Zucker, S., & Mazeh, T. 2002, Astronomy and Astrophysics, 391, 369

Kowalski, A. F., Hawley, S. L., Hilton, E. J., Becker, A. C., West, A. A., et al. 2009, The Astronomical Journal, 138, 633

Kraus, A. L., Cody, A. M., Covey, K. R., Rizzuto, A. C., Mann, A. W., et al. 2015, The Astrophysical Journal, 807, 3

Law, N. M., Kulkarni, S. R., Dekany, R. G., Ofek, E. O., Quimby, R. M., et al. 2009, Publications of the Astronomical Society of the Pacific, 121, 1395

Lawrence, J. S., Ashley, M. C. B., Hengst, S., Luong-van, D. M., Storey, J. W. V., et al. 2009, Review of Scientific Instruments, 80, 064501

Lomb, N. R. 1976, Astrophysics and Space Science, 39, 447

Lopez Martí, B., Jimenez Esteban, F., Bayo, A., Barrado, D., Solano, E., et al. 2013, Astronomy and Astrophysics, 551, A46

Luhman, K. L., & Mamajek, E. E. 2012, The Astrophysical Journal, 758, 31

Lurie, J. C., Davenport, J. R. A., Hawley, S. L., Wilkinson, T. D., Wisniewski, J. P., et al. 2015, The Astrophysical Journal, 800, 95

Mamajek, E. E. 2009, in American Institute of Physics Conference Series, Vol. 1158, American Institute of Physics Conference Series, ed. T. Usuda, M. Tamura, &

M. Ishii, 3–10

Mamajek, E. E., Lawson, W. A., & Feigelson, E. D. 1999, The Astrophysical Journal Letters, 516, L77

Mayor, M., & Queloz, D. 1995, Nature, 378, 355

Meng, Z., Zhou, X., Zhang, H., Zhou, J., Wang, S., et al. 2013, Publications of the Astronomical Society of the Pacific, 125, 1015

Miller, J. P., Pennypacker, C. R., & White, G. L. 2008, Publications of the Astronomical Society of the Pacific, 120, 449

Morales-Calderón, M., Stauffer, J. R., Stassun, K. G., Vrba, F. J., Prato, L., et al. 2012, The Astrophysical Journal, 753, 149

O'Connell, D. J. K. 1951, Publications of the Riverview College Observatory, 2, 85

Oelkers, R. J., Macri, L. M., Wang, L., Ashley, M. C. B., Cui, X., et al. 2015, The Astronomical Journal, 149, 50

Ofek, E. O. 2008, Publications of the Astronomical Society of the Pacific, 120, 1128

Pecaut, M. J., & Mamajek, E. E. 2013, The Astrophysical Journal, 208, 9

Pecaut, M. J., Mamajek, E. E., & Bubar, E. J. 2012, The Astrophysical Journal, 746, 154

Pepper, J., Pogge, R. W., DePoy, D. L., Marshall, J. L., Stanek, K. Z., et al. 2007, Publications of the Astronomical Society of the Pacific, 119, 923

Pietrinferni, A., Cassisi, S., Salaris, M., & Castelli, F. 2006, The Astrophysical Journal, 642, 797

Pollacco, D. L., Skillen, I., Collier Cameron, A., Christian, D. J., Hellier, C., et al. 2006, Publications of the Astronomical Society of the Pacific, 118, 1407

Pont, F., Zucker, S., & Queloz, D. 2006, Monthly Notices of the Royal Astronomical Society, 373, 231

Preibisch, T., Brown, A. G. A., Bridges, T., Guenther, E., & Zinnecker, H. 2002,

The Astronomical Journal, 124, 404

Qian, S.-B., Wang, J.-J., Zhu, L.-Y., Snoonthornthum, B., Wang, L.-Z., et al. 2014, The Astrophysical Journal Supplement Series, 212, 4

Reipurth, B. 2008, Handbook of Star Forming Regions, Volume II: The Southern Sky (San Francisco: Astronomical Society of the Pacific), 878

Rizzuto, A. C., Ireland, M. J., & Kraus, A. L. 2015, Monthly Notices of the Royal Astronomical Society, 448, 2737

Scargle, J. D. 1982, The Astrophysical Journal, 263, 835

Schlafly, E. F., & Finkbeiner, D. P. 2011, The Astrophysical Journal, 737, 103

Skrutskie, M. F., Cutri, R. M., Stiening, R., Weinberg, M. D., Schneider, S., et al. 2006, The Astronomical Journal, 131, 1163

Southworth, J., Mancini, L., Browne, P., Burgdorf, M., Calchi Novati, S., et al. 2013, Monthly Notices of the Royal Astronomical Society, 434, 1300

Spada, F., Demarque, P., Kim, Y.-C., & Sills, A. 2013, The Astrophysical Journal, 776, 87

Stassun, K. G., Feiden, G. A., & Torres, G. 2014, New Astronomy Reviews, 60, 1

Stetson, P. B. 1987, Publications of the Astronomical Society of the Pacific, 99, 191

—. 1996, Publications of the Astronomical Society of the Pacific, 108, 851

Torres, G., Andersen, J., & Giménez, A. 2010, Astronomy and Astrophysics Reviews, 18, 67

van Eyken, J. C., Ciardi, D. R., von Braun, K., Kane, S. R., Plavchan, P., et al. 2012, The Astrophysical Journal, 755, 42

Wang, D., Foreman-Mackey, D., Hogg, D. W., & Schölkopf, B. 2015, ArXiv e-prints, arXiv:1508.01853

Wang, L., Macri, L. M., Krisciunas, K., Wang, L., Ashley, M. C. B., et al. 2011, The Astronomical Journal, 142, 155

Wang, L., Macri, L. M., Wang, L., Ashley, M. C. B., Cui, X., et al. 2013, The Astronomical Journal, 146, 139

Wang, S., Zhou, X., Zhang, H., Zhou, J., Ma, J., et al. 2012, Publications of the Astronomical Society of the Pacific, 124, 1167

Wang, S., Zhang, H., Zhou, J.-L., Zhou, X., Yang, M., et al. 2014, The Astrophysical Journal Supplement Series, 211, 26

Wang, S., Zhang, H., Zhou, X., Zhou, J.-L., Fu, J.-N., et al. 2015, The Astrophysical Journal Supplement Series, 218, 20

Wang, S.-H., Zhou, X., Zhang, H., Zhou, J.-L., Liu, H.-G., et al. 2014, Research in Astronomy and Astrophysics, 14, 345

Wright, E. L., Eisenhardt, P. R. M., Mainzer, A. K., Ressler, M. E., Cutri, R. M., et al. 2010, The Astronomical Journal, 140, 1868

Yang, M., Zhang, H., Wang, S., Zhou, J.-L., Zhou, X., et al. 2015, The Astrophysical Journal Supplement Series, 217, 28

Young, A. T. 1967, The Astronomical Journal, 72, 747

Yu, L., Winn, J. N., Gillon, M., Albrecht, S., Rappaport, S., et al. 2015, The Astrophysical Journal, 812, 48

Yuan, X., Cui, X., Liu, G., Zhai, F., Gong, X., et al. 2008, in Society of Photo-Optical Instrumentation Engineers (SPIE) Conference Series, Vol. 7012, Society of Photo-Optical Instrumentation Engineers (SPIE) Conference Series

Zacharias, N., Finch, C. T., Girard, T. M., Henden, A., Bartlett, J. L., et al. 2013, The Astronomical Journal, 145, 44

Zhou, X., Wu, Z.-Y., Jiang, Z.-J., Cui, X.-Q., Feng, L.-L., et al. 2010a, Research in Astronomy and Astrophysics, 10, 279

Zhou, X., Fan, Z., Jiang, Z., Ashley, M. C. B., Cui, X., et al. 2010b, Publications of the Astronomical Society of the Pacific, 122, 347

Zhou, X., Ashley, M. C. B., Cui, X., Feng, L., Gong, X., et al. 2013, in IAU Symposium, Vol. 288, IAU Symposium, ed. M. G. Burton, X. Cui, & N. F. H. Tothill, 231–238

Zou, H., Zhou, X., Jiang, Z., Ashley, M. C. B., Cui, X., et al. 2010, The Astronomical Journal, 140, 602